IRAQI JOURNAL OF APPLIED PHYSICS

The *Iraqi Journal of Applied Physics (IJAP)* is a peer reviewed journal of high quality devoted to the publication of original research papers from applied physics and their broad range of applications. IJAP publishes quality original research papers, comprehensive review articles, survey articles, book reviews, dissertation abstracts in physics and its applications in the broadest sense. It is intended that the journal may act as an interdisciplinary forum for Physics and its applications. Innovative applications and material that brings together diverse areas of Physics are particularly welcome. Review articles in selected areas are published from time to time. It aims to disseminate knowledge; provide a learned reference in the field; and establish channels of communication between academic and research experts, policy makers and executives in industry, commerce and investment institutions. IJAP is a quarterly specialized periodical dedicated to publishing original papers, letters and reviews in: Applied & Nonlinear Optics, Applied Mechanics & Thermodynamics, Digital & Optical Communications, Electronic Materials & Devices, Laser Physics & Applications, Plasma Physics & Applications, Quantum Physics & Spectroscopy, Semiconductors & Optoelectronics, and Solid State Physics & Applications

EDITORIAL BOARD

Dayah N. RAOUF
Editor-in-Chief
School of Applied Sciences
University of Technology, IRAQ
dayah@ijap.org

Walid K. HAMOUDI
Member
School of Applied Sciences,
University of Technology, IRAQ
walid@ijap.org

Raid A. ISMAIL
Member
Ministry of Science and
Technology, Baghdad, IRAQ
raid@ijap.org

Raad A. KHAMIS
Member
School of Applied Sciences
University of Technology, IRAQ
raad@ijap.org

Oday A. HAMADI
Managing Editor
P. O. Box 55159,
Baghdad 12001, IRAQ
oday@ijap.org

Rania A. MARKUB
Middle East Coordinator
P. O. Box 55259,
Baghdad 12001, IRAQ
rania@ijap.org

Haitham M. MIKHLIF
Reviews Editor
Department of Physics,
Al-Mustansiriya University, IRAQ
haitham@ijap.org

Intesar F. RAMLEY
Industrial Relation Coordinator
INToo Software, Vancouver,
V4B 4W4, BC, Canada
intesar@ramley.com

Editorial Office
P. O. Box 55259,
Baghdad 12001,
IRAQ
Website: **www.ijap.org**
Email: **editor@ijap.org**
Tel.: **00964 7901274190**

ADVISORY BOARD

Xueming LIU
Professor
Department of Electronic Engineering,
Tsinghua University, Beijing, CHINA

Mansoor SHEIK-BAHAE
Associate Professor
Department of Physics and Astronomy,
University of New Mexico, U.S.A

Shivaji H. PAWAR
Professor
D. Y. Patil University, Kasaba Bawada,
Kolhapur-416 006, INDIA

Franko KUEPPERS
Professor
College of Optical Sciences,
University of Arizona, Tucson, U.S.A

Yushihiro TAGUCHI
Professor
Department of Physics, Chuo University,
Bunkyo-ku, Tokyo, JAPAN

El-Sayed M. FARAG
Professor
Department of Sciences, College of
Engineering, Al-Minofiya University, EGYPT

Mutaz S. ABDUL-WAHAB
Assistant Professor
Electric and Electronic Engineering,
University of Technology, Baghdad, IRAQ

Mazin M. ELIAS
Professor
Laser Institute for Postgraduates
University of Baghdad, Baghdad, IRAQ

Kais A. AL-NAIMEE
Assistant Professor
National Institute of Applied Optics, Phys.
Dep., University of Florence, Florence, Italy

Muhammad A. HUSSAIN
Assistant Professor
Department of Laser and Optoelectronics
Engineering, Al-Nahrain University, IRAQ

Chang Hee NAM
Professor
Korean Advanced Institute of Science
and Technology, Taejon, KOREA

Ashok KUMAR
Professor
Harcourt Butler Technological Institute,
Kanpur-208 002, INDIA

Marc BURGELMAN
Professor
Electronics and Information Systems,
University of Gent, Gent, BELGIUM

Heidi ABRAHAMSE
Professor
Faculty of Health Sciences, University
of Johannesburg, SOUTH AFRICA

Andrei KASIMOV
Professor
Institute of Material Science, National
Academy of Science, UKRAINE

Yanko SAROV
Assistant Professor
Micro- and Nanoelectronic Systems,
Technical University Ilmenau, GERMANY

Mohammed A. HABEEB
Professor
Department of Physics, Faculty of
Science, Al-Nahrain University, IRAQ

Abdullah M. SUHAIL
Assistant Professor
Department of Physics, College of
Science, University of Baghdad, IRAQ

Khaled A. AHMED
Assistant Professor
Department of Physics, College of Science,
Al-Mustansiriya University, IRAQ

Manal J. AL-KINDY
Assistant Professor
Department of Electronic Engineering,
Al-Nahrain University, IRAQ

SPONSORED AND PUBLISHED BY
THE IRAQI SOCIETY FOR ALTERNATIVE AND RENEWABLE ENERGY SOURCES & TECHNIQUES (I.S.A.R.E.S.T.)

IRAQI JOURNAL OF APPLIED PHYSICS
" INSTRUCTIONS TO AUTHORS "

CONTRIBUTIONS

Contributions to be published in this journal should be original research works, i.e., those not already published or submitted for publication elsewhere, individual papers or letters to editor.

SUBMISSION OF MANUSCRIPTS

Manuscripts should be submitted to the editor at the mailing address:

Iraqi Journal of Applied Physics
Editorial Board
P. O. Box 55259, Baghdad 12001, IRAQ, submission@ijap.org , editor@ijap.org

MANUSCRIPTS

Two hard copies with soft copy on a compact disc (CD) should be submitted to Editor in the following configuration:

- Double-spaced one-side A4 size with 2.5 cm margins of all sides
- Times New Roman font (16pt bold for title, 14pt bold for names, 12pt bold for headings, 12pt regular for text)
- Letters should not exceed 10 pages, papers should not exceed 20 pages and reviews are up to author.
- Manuscripts presented in English only are accepted.
- English abstract not exceed 150 words
- 4 keywords (at least) should be maintained on (PACS preferred)
- Author(s) should express all quantities in SI units
- Equations should be written in equation form (*italic* and symbolic)
- Figures and Tables should be separated from text
- Figures and diagrams can be submitted in colors for assessment and they will be returned to authors after provide printable copies
- Charts should be indicated by the software used for
- Only original or high-resolution scanner photos are accepted
- For electronic submission, articles should be formatted with MS-Word software.

AUTHOR NAMES AND AFFILIATIONS

It is IJAP policy that all those who have participated significantly in the technical aspects of a paper be recognized as co-authors or cited in the acknowledgments. In the case of a paper with more than one author, correspondence concerning the paper will be sent to the first author unless staff is advised otherwise.

Author name should consist of first name, middle initial, last name. The author affiliation should consist of the following, as applicable, in the order noted:

- Company or college (with department name or company division)
- Postal address
- City, state, zip code
- Country name
- Telephone, and e-mail

REFERENCES

The references should be brought at the end of the article, and numbered in the order of their appearance in the paper. The reference list should be cited in accordance with the following examples:

[1] X. Ning and M.R. Lovell, "On the Sliding Friction Characteristics of Unidirectional Continuous FRP Composites", *ASME J. Tribol.*, 124(1) (2002) 5-13.
[2] M. Barnes, "Stresses in Solenoids", *J. Appl. Phys.*, 48(5) (2001) 2000–2008.
[3] J. Jones, "Contact Mechanics", Cambridge University Press (Cambridge, UK) (2000), Ch.6, p.56.
[4] Y. Lee, S.A. Korpela and R. Horne, "Structure of Multi-Cellular Natural Convection in a Tall Vertical Annulus", Proc. 7th International Heat Transfer Conference, U. Grigul et al., eds., Hemisphere (Washington DC), 2 (1982) 221–226.
[5] M. Hashish, "Waterjet Technology Development", High Pressure Technology, PVP-Vol. 406 (2000), 135-140.
[6] D.W. Watson, "Thermodynamic Analysis", ASME Paper No. 97-GT-288 (1997).
[7] C.Y. Tung, "Evaporative Heat Transfer in the Contact Line of a Mixture", Ph.D. thesis, Rensselaer Polytechnic Institute, Troy, NY (1982).

PROOFS

Authors will receive proofs of papers and are requested to return one corrected hard copy with a WORD copy on a compact disc (CD). New materials inserted in the original text without Editor permission may cause rejection of paper.

COPYRIGHT FORM

Author(s) will be asked to transfer copyrights of the article to the Journal soon after acceptance of it. This will ensure the widest possible dissemination of information.

OFFPRINTS

Authors will receive offprints free of charge and any additional offprints can be ordered.

SUBSCRIPTION AND ORDERS

Annual fees (4 issues per year) of subscription are:

- 50 US$ for individuals inside Iraq.
- 100 US$ for establishments inside Iraq.
- 100 US$ for individuals abroad.
- 200 US$ for establishments abroad.

Fees are reduced by 25% for I.S.A.R.E.S.T. members. Orders of issues can be submitted by contacting the editor-in-chief or editorial office at **subscription@ijap.org** to maintain the address of issue delivery and payment way.

Performance Optimizing of Fourth Order Delta-Sigma Fractional-N Frequency Synthesizer using a Dither Technique for Third Generation (3G) Applications

Mithaq N. Raheema
Hassan A. Nasir
Ali K. Naher

Department of Electrical and Electronic Engineering, University of Technology, Baghdad, Iraq

This paper proposes a frequency synthesizer for WCDMA applications. Different techniques for phase noise reduction are discussed. Sigma-delta fractional-N technique is chosen for WCDMA system, since low settling time, spurious level and phase noise can be obtained by using this technique. Also it is proposed to add dither before the quantizer of modulator in order to eliminate any distortions introduced by the quantization stage. Design parameters for the proposed 4^{th} order (1-1-1-1) MASH fractional-N synthesizer for 3G are selected from the results of analysis for each unit of the proposed system and according to WCDMA standards. Simulation results prove that the proposed dithered frequency synthesizer for the WCDMA application is very efficient in reducing noise. The in-band phase noise obtained with this synthesizer is -96dBc/Hz. MATLAB (R2010a) are used for simulation of MASH (1-1-1-1) fractional-N frequency synthesizer.

Keywords: UMTS, WCDMA, Frequency synthesizer, Dither, MASH
Received: 9 January 2011, **Revised**: 24 March 2011, **Accepted**: 31 March 2011

1. Introduction

The most important network technology for third generation (3G) is UMTS (Universal Mobile Telecommunications System). UMTS is a European concept for integrated mobile services and it is based on the GSM and GPRS. It provides a wide range of mobile services wherever the user is located and multimedia service with data rates up to 2 Mbps. The cellular radio access method for UMTS is wideband CDMA (WCDMA). The new frequency band at the 2-GHz range is allocated for UMTS. The channel bandwidth is 5 MHz, and each channel is used by all cells [1]. However, common to almost all of these standards is that the data to be transferred is somehow modulated on a radio frequency (RF) carrier, and the modulated signal is then transmitted over the air. The received signal is demodulated in the receiving end, an accurate RF carrier signal must be generated. Therefore, a frequency synthesizer is required in transmitter and receiver for all wireless communication systems. Most important part to all wireless systems is frequency synthesizer (FS). A FS is a device that generates one or many frequencies from one or a few frequency sources. Practically all communication systems use local oscillator (LO) based on frequency synthesis [2].

The FS is used in the receiver or transmitter, as a part of a larger radio communication system. The receiver must be sensitive, selective, and able to detect even a weak signal among many other, possibly stronger signals. Therefore, a good receiver must have an accurate local oscillator frequency and low-noise components. However, a transmitter must produce a signal that has enough power, very accurate frequency and clean enough spectrum. Most synthesizers in RF applications are based on the phase-locked loop (PLL) principle, as shown in Fig. (1), the basic PLL is made up of four building blocks [3]: Phase-frequency detector (PFD), charge pump (CP) with low pass filter (LPF), VCO, and a divider. An output signal of frequency f_{out} is generated, and f_{out} is divided by N. The output of the divider is a signal with low frequency (f_{out} /N), which is sent to the PFD. At the PFD, the phas and frequency of the signal are compared with an external signal of frequency (f_{Ref}), which is generated using a crystal oscillator. The output signal of the PFD and CP is then low pass filtered, and the filtered signal is sent to the VCO input to control the frequency of the output signal. The disadvantage of this technique is the output frequency is equal to multiple of the reference frequency (f_{out}=N$x f_{\mathrm{Ref}}$), where N, the loop frequency divide ratio, is an integer. The frequency resolution of the integer-N FS is equal to the reference frequency. The conventional integer-N PLL with low reference frequency has several disadvantages. First, the lock time is long due to its narrow loop-bandwidth. Second, the reference spur and its harmonics are located at low offset frequencies. Third, the large divide ratio (N) increases the in-band phase noise associated with the reference signal. Finally, with a small loop-bandwidth, the phase noise of the VCO will not be sufficiently suppressed at low offset frequencies. The most well accepted solution to these problems is the fractional-N PLL that will be discussed in the next section.

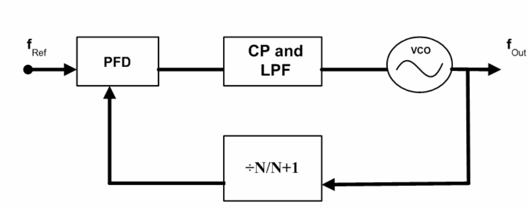

Fig. (1) The block diagram of phase-locked loop [3]

2. Fractional-N Frequency Synthesizer

In integer-N synthesizer, the minimum resolution is equal to the reference frequency. In order to get a finer resolution, a fractional-N technique is used to achieve frequency resolution finer than the reference frequency, as shown in Fig. (2a). The output frequency f_{out} can be varied in fractional increments of reference frequency. The fractional part of divider is implemented using phase accumulator.

The main source of problems in fractional-N synthesizers is when an overflow occurs in the accumulator, the divider ($\div N/N{+}1$) is divided by N+1 for one period, corresponding to a 2π decrease in the phase error at the phase detector input, as shown in Fig. (2b). The resulting phase error causes spurious tones at the output frequency [3].

2.1 Spur-Suppression Techniques

The classical approach to fractional-N synthesizer design employs dithering and phase interpolation (PI), as shown in Fig. (3). An accumulator carry-out signal is used to dither the control input to a multi modulus divider. The DAC is used to convert the instantaneous phase error, which is proportional to the residue of the accumulator, into an equivalent amount of charge-pump current to compensate the phase error [4,5]. The main limitation with this architecture centers on the achievement of a good matching between the DAC output and phase-error signal. This matching is difficult to obtain because the two signals are processed by separate circuits whose outputs are summed. Any gain mismatch between PFD error and DAC output will lead to spurious tones at PLL output [3]. The second technique uses a delta-sigma modulator. This technique is based on oversampling ratio (OSR) and noise shaping to reduce the phase noise, as shown in Fig. (4) [3].

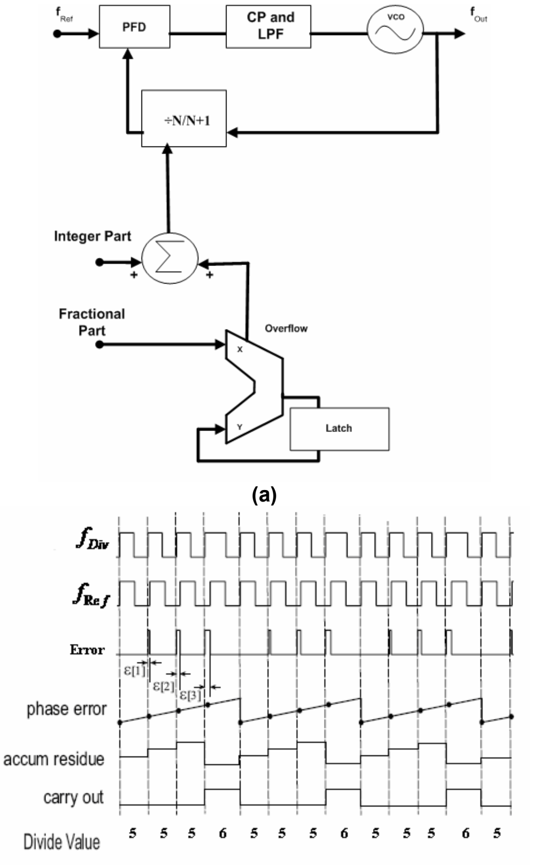

(b)

Fig. (2) (a) Classical fractional-N synthesizer, (b) Accumulation process (fraction=0.25) [8]

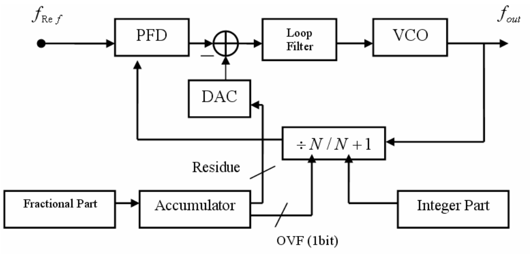

Fig. (3) Phase interpolation technique [3]

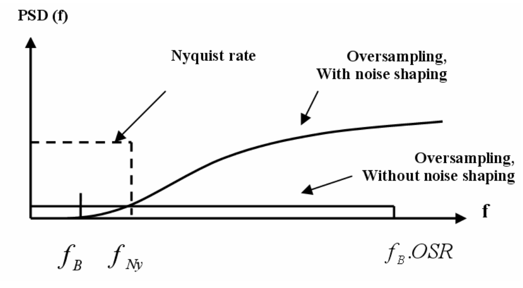

Fig. (4) The power spectral density of the quantization noise [6]

3. Modulator analysis

As shown in Fig. (5a), its name (ΔΣ) is derived from the difference and summing nodes in a loop configuration, where "delta (Δ)" denotes the difference operation made in the input node, and "sigma (Σ)" denotes the summation (accumulation).

In the linear model of the ΔΣ modulator illustrated in Fig. (5b), the modulator output can be described by using the superposition principle as[6] :

$$V(z) = (U(z) - V(z)).H(z) + Q(z) \qquad (1)$$

$$V(z) = \frac{H(z)}{1+H(z)}.U(z) + \frac{1}{1+H(z)}.Q(z) \qquad (2)$$

where H(z)=$Z^{1}/(1-Z^{1})$

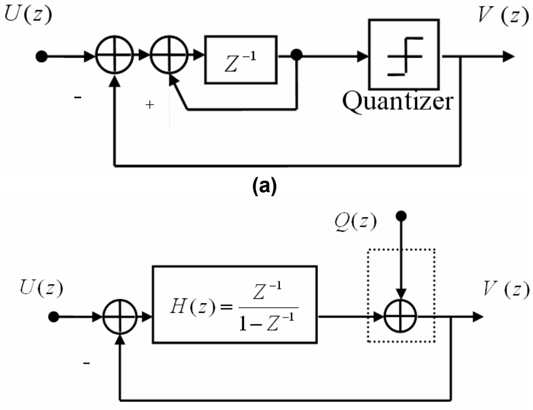

(a)

(b)

Fig. (5) (a) First order sigma-delta modulator (b) its linearized model [6]

Two transfer functions are used to determine modulator performance, a Signal Transfer Function (STF) of the system and a Noise Transfer Function (NTF) of the system. These transfer functions are given by:

$$STF(z) = \frac{V(z)}{U(z)}\Big|_{Q(z)=0} = \frac{H(z)}{1+H(z)} = Z^{-1} \qquad (3)$$

$$NTF(z) = \frac{V(z)}{Q(z)}\Big|_{U(z)=0} = \frac{1}{1+H(z)} = (1-Z^{-1}) \qquad (4)$$

Substituting equations (3) and (4) by equation (2), the loop output is determined as:

$$V(z) = U(z).Z^{-1} + Q(z).(1-Z^{-1}) \qquad (5)$$

The STF and NTF for high order sigma-delta modulator is given by Eq. (6):

$$V(z) = U(z).Z^{-L} + Q(z).(1-Z^{-1})^{L} \qquad (6)$$

where L is the ordr of the sigma -delta modulator

3.1 Cascaded ΣΔ Modulators (MASH) Description

Cascaded ΣΔ modulators are suitable for high-resolution and large-bandwidth applications [7]. The general structure of a cascaded fourth order ΣΔ or Multi-stAge noiSe-sHaping (MASH) modulator is presented in Fig. (6). The cascaded modulator can be obtained by interconnecting four delta-sigma modulators, the input is fed to a modulator and then the quantization error from this one is fed to a new modulator and so on. As shown in equations (1)-(5), the output of the first modulator is:

$$V_1(z) = U\ (z).Z^{-1} + Q_1(z).(1-Z^{-1}) \qquad (7)$$

Feeding the (Q_1) of the first modulator into the input of the second stage, the output of the second stage, is:

$$V_2(z) = z^{-1}.Q_1(z) + (1-z^{-1}).Q_2(z) \qquad (8)$$

where $Q_2(z)$ is a quantization noise of the second modulator. The outputs of the third and fourth modulators are:

$$V_3(z) = Q_2(z).Z^{-1} + Q_3(z).(1-Z^{-1}) \qquad (9)$$

$$V_4(z) = Q_3(z).Z^{-1} + Q_4(z).(1-Z^{-1}) \qquad (10)$$

Combining the outputs of all modulators, the output of the entire modulator is given by:

$$V(z)=V_1(z)H(Z)+V_2(z)H_1(Z)+V_3(z)H_2(Z)+V_4.H_3(Z) \qquad (11)$$

where:

$$H(Z) = Z^{-4}$$

$$H_1(Z) = (1-Z^{-1})$$

$$H_2(Z) = (1-Z^{-1})^2$$

$$H_3(Z) = (1-Z^{-1})^3$$

The final output of the modulator is given by Eq. (12):

$$V(Z) = Z^{-4}.U(Z) + Q_4(Z).(1-Z^{-1})^4 \qquad (12)$$

As equation (12) shows, the quantization noise of the first modulator cancels out. This greatly improves the reduction of quantization noise of the modulator.

4. Dithering Technique

Dithering in Δ□ modulator is the act of adding a random (or pseudorandom) signal to the input of the quantizer (not to the modulator input) as shown in Fig. (6). The added random signal is white, it also becomes noise shaped like the quantization error so that the additional noise power in baseband is minimized. The purpose of dithering is to effectively decorrelate and whiten the quantization error [8].

5. The Description of the Proposed Frequency Synthesizer

Figure (7) shows the flow chart of the program used to design the proposed dithered fractional-N PLL synthesizer for WCDMA applications. The design parameters are listed in table (1), which are either selected from WCDMA standards or according to the result analysis of each unit of the proposed system.

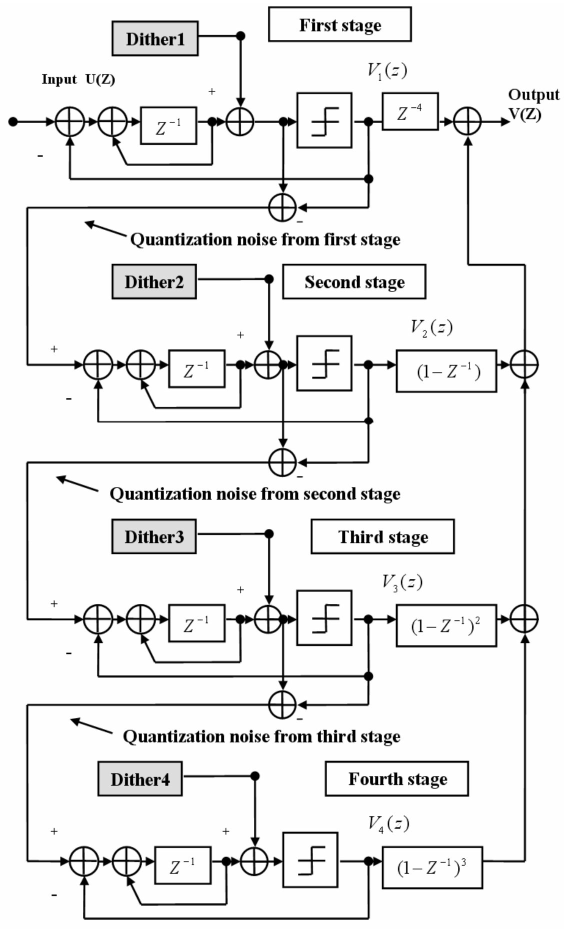

Fig. (6) Proposed 4th order Δ modulator type (MASH 1-1-1-1) with dither

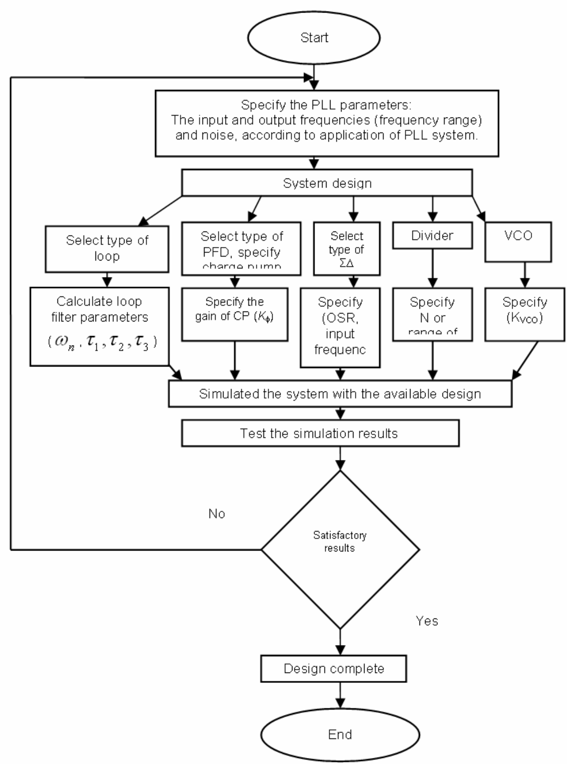

Fig. (7) Flow chart of the simulation program

6. Simulation Results

6.1 Quantization Noise Simulation

Figure (8) shows the simulation results of the proposed ΔΣ MASH modulator and the single loop 4th order modulator was designed in [9] for comparison. The quantization noise of fourth MASH ΔΣ modulator is perfectly cancelled by using dither technique. However, the fourth order ΔΣ MASH is suggested to eliminate quantization noise and spurs. The net improvement in quantization noise reduction is 8 dB if compared with single-loop fourth order was designed in [9].

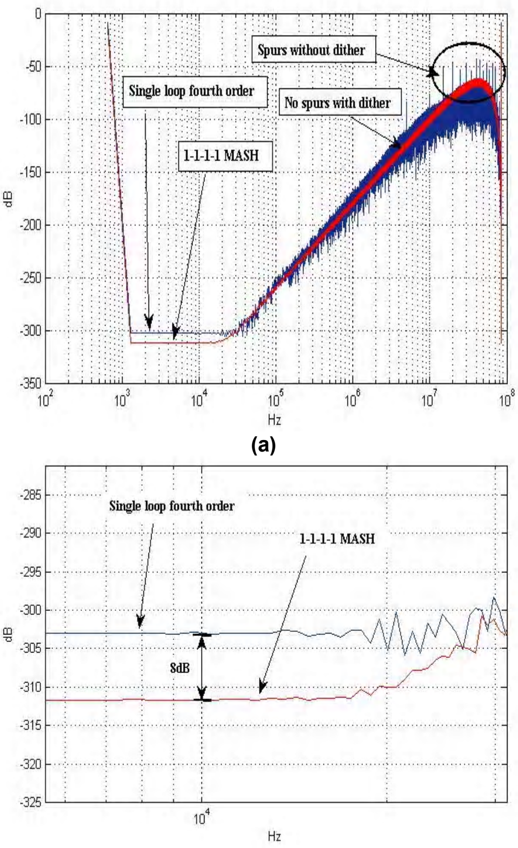

(a)

(b)

Fig. (8) (a) Simulation of quantization noise spectrum of the proposed 4th order (1-1-1-1) MASH modulator and the single loop 4th order modulator designed in [9], (b) Zoom-in

6.2 Phase Noise Simulation

Figure (9) shows the final simulation result of the 4th order MASH fractional-N synthesizer. The broadband noise is greatly reduced achieving high levels of fraction spur rejection at the output spectrum of PLL.

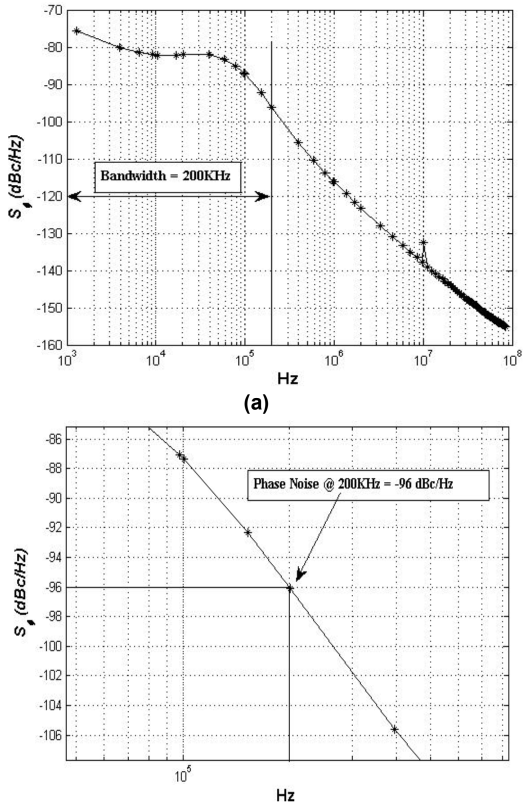

(a)

(b)

Fig. (9) (a) final output spectrum of MASH (1-1-1-1) synthesizer for WCDMA (b) Zoom-in

The overall phase noise performance of the synthesizer is good as shown in Fig. (9). It meets the equivalent of the WCDMA requirements at 1.965 GHz, and meets the reduced spurious goal. Also these results show the effectiveness of the proposed system in reduction of the phase noise and spurs. As compression with [9] the net improvement in phase noise is 4dBc/Hz in-band, as shown in Fig. (9). Table (2) summarizes the final phase noise results of the proposed ΔΣ fractional-N PLL compared with [9].

Table (1) The basic requirements of Δ modulator, CP, filter, and VCO

Unit	Parameters	Value
Δ modulator	order	Fourth
	type	MASH (1-1-1-1) with dither
	Bus size (N=accumulator bits)	26 bit
Charge-pump	current	0.45 mA
Filter	Butterworth	Passive
	Type	Two (II)
	order	third
VCO	Corner Frequency	0.5MHz
	Noise Figure	9
	VCO sensitivity (K_{VCO})	55 MHz/V

Table (2) Summary of simulation results

Parameter	Proposed system	Ref. [9]	Note
Output frequency	1.965GHz	1.965GHz	WCDMA Spectrum
Loop bandwidth	200KHz	200KHz	
In-band phase noise for BW=200 KHz	-96 dBc/Hz	-92 dBc/Hz	The net improvement of noise reduction (In-band) = 4dBc/Hz
out-band phase noise for BW=3.5 MHz	-129 dBc/Hz	-128 dBc/Hz	The net improvement of noise reduction (out-band) = 1dBc/Hz
Spur	No spur	-66 dBc/-71dBc	No spur at modulator output due to dither.
Reference frequency	85MHz	26MHz	Large reference frequency for good tradeoff with settling time
No. of bits (N)	26	20	Increase resolution
Resolution ($f_{Ref}/2^N$)	<10	<100	Step size or frequency resolution: The smallest frequency difference possible between any two adjacent output frequencies.
ΣΔ modulator	MASH 1-1-1-1 with dither	Fourth/five Single loop high-order	• Single loop high order unstable [8]. • MASH guaranteed stability [8].
Quantizer	(1) bit	(3-4) bit	

6.3 Stability of 4th (1-1-1-1) order MASH fractional-N synthesizer PLL and Setling Time Simulation Results

Figure (10) shows simulation results of the open-loop frequency response. The crossover frequency is 384.7 krad/s and the phase margin is 52°. Since the phase margin is greater than 45 degrees, the system is stable. The step response is performed to check the settling time of the PLL is below 30µsec, as shown in Fig. (11).

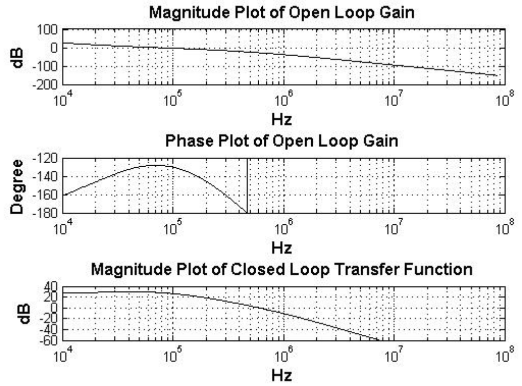

Fig. (10) Open-loop response of the proposed 4th (1-1-1-1) order MASH fractional-N synthesizer

7. Conclusions

The 4th order MASH (1-1-1-1) fractional-N synthesizer is designed to generate 1965 MHz, with following main characteristics:

- Phase noise is -96 dBc/Hz in band
- Phase noise is -129 dB/Hz out of band
- Bandwidth of system is 200 KHz
- Settling time < 30 µs

MASH modulator fractional-N technique is selected to WCDMA system since it has the following advantages:

- Short settling time
- Step size smaller than an integer-N PLL

The quantization noise of modulator is perfectly cancelled by using 4th order MASH (1-1-1-1) modulator.

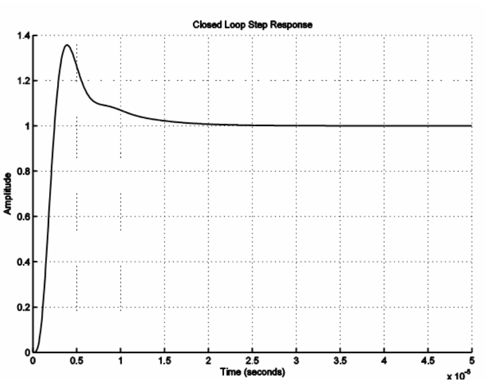

Fig. (11) Step response of Δ PLL synthesizer

References

[1] T. Anttalainen, **"Introduction to Telecommunications Network Engineering"**, Artech House (2003).

[2] A.V. Raisanen and A. Lehto, **"Radio Engineering for Wireless Communication and Sensor Applications"**, Artech House (2003).

[3] K. Shu and E.S. Sinencio, **"CMOS PLL Synthesizers: Analysis and Design"**, Springer, Inc. (2005).

[4] S.E. Meninger and M.H. Perrott, *IEEE Trans. on Circuits and Systems II: Analog and Digital Signal Processing*, 50(11) (2003) 839-849.

[5] L. Jansson, S. Pamarti and I. Galton, *IEEE Trans. on Circuits and Systems II: Analog and Digital Signal Processing*, 39(1) (2004) 49-62.

[6] S. Park, **"Principles of Sigma-Delta Modulation for Analog-to-Digital Converters"**, Motorola, Inc., Application Note APR8 (1997).

[7] P. Kiss, "Adaptive Digital Compensation of Analog Circuit Imperfections for Cascaded Delta-Sigma A/D Converters", Ph.D. thesis, Oregon State University (1999).

[8] M. Kozak and I. Kale, **"Oversampled Delta-Sigma Modulators, Analysis, Applications and Novel Topologies"**, Kluwer Academic Publishers (2003).

[9] X. Yu et al., *IEEE Custom Integrated Circuits Conf.* (CICC) (2008) 753-756.

Call for Papers

ITC-CSCC 2011

The 26th International Technical Conference on Circuits/Systems, Computers and Communications

June 19 – 22, 2011 / Hyundai Hotel, Gyeongju, Korea / http://www.itc-cscc2011.org

----

The 26th International Technical Conference on Circuits/Systems, Computers and Communications (ITC-CSCC 2011) will be held on June 19-22 at Hyundai Hotel in Gyeongju , Korea . We would like to invite all the scholars and experts around the world to attend the conference to be hosted at the wonderful city of Korea . The meetings at Shimonoseki in 2008, Jeju in 2009, Pattaya in 2010 were successfully held in this world leading conference devoted to the advancement of high technologies in Circuits/Systems, Computers and Communications.

Topics

The conference is open to researchers from all regions of the world. Participation from Asia Pacific region is particularly encouraged. Proposals for special sessions are welcome. Papers with original works in all aspects of Circuits/Systems, Computers and Communications are invited. Topics include, but not limited to, the followings:

Circuits & Systems
- Analog Circuits
- Computer Aided Design
- Intelligent Transportation Systems & Technology
- Linear / Nonlinear Systems
- Medical Electronics & Circuits
- RF Circuits
- Semiconductor Devices and Technology
- Power Electronics & Circuits
- Modern Control
- Neural Networks
- VLSI Design
- Verification and Testing

Computers
- Artificial Intelligence
- Biocomputing
- Computer Systems & Applications
- Computer Vision
- Face Detection & Recognition
- Image Coding & Analysis
- Image Processing
- Internet Technology & Applications
- Motion Analysis
- Multimedia Service & Technology
- Object Extraction & Technology
- Security
- Watermarking

Communications
- Antenna & Wave Propagation
- Audio / Speech Signal Processing
- Circuits & Components for Communications
- IP Networks & QoS
- MIMO & Space-Time Codes
- Multimedia Communications
- Mobile & Wireless Communications
- Network Management & Design
- Optical communications and Components
- Radar / Remote Sensing
- Communication Signal Processing
- Ubiquitous Networks
- UWB
- Visual Communications

Submission of Papers

Prospective authors are invited to submit original paper(s) of either MS Word or PDF format written in English. Abstract is limited to two pages of text and figures. Abstract can be submitted on the official website (http://www.itc-cscc2011.org). If you have any trouble in preparing papers and online submission, please contact the conference secretariat.

Proceedings

All registered participants are provided with conference proceedings. Moreover, authors of the accepted papers are encouraged to submit full-length manuscripts to IEEK JSTS (Journal of Semiconductor Technology and Science) or IEICE Transactions. Papers passed through the standard review procedures of the IEEK JSTS or IEICE Transactions will be published in regular issues. The authors (or their institute) are requested to pay the publication charge for the IEICE Transactions when their paper is accepted.

Important Dates

Submission of Abstract: Extended to April 14, 2011
Notification of Acceptance: April 30, 2011
Submission of Camera Ready Paper: May 15, 2011

Plenary

Applications of Sparse and Redundant Representations in Signal Processing
Prof. Aggelos K. Katsaggelos *(Northwestern University , USA)*
Future Technology of Medical Imaging Devices
Dr. Jaemoon Jo *(Samsung Electronics , Korea)*
Present Status and Future Trend of PI/SI/EMI Simulation Technology for High-Speed Electronic Design
Prof. Hideki Asai *(Shizuoka University , Japan)*
Microwave for Agricultural Applications
Prof. Monai Krairiksh *(King Mongkut's Institute of Technology Ladkrabang , Thailand)*

Conference Venue and City

Gyeongju is a coastal city in the far southeastern corner of North Gyeongsang province in South Korea. It is the second largest city by area in the province, covering 1,300 km2 with a population of 270,000 people. Gyeongju is 370 km southeast of Seoul, and 60 km north of Busan. Numerous low mountains are scattered around the city. Gyeongju was the capital of the ancient kingdom of Silla (57 BC – 935 AD) which ruled most of the Korean Peninsula between the 7th and 9th centuries. A vast number of archaeological sites and cultural heritages from this period remain in the city. Gyeongju is often referred to as "the museum without walls." Among such historical treasures, Seokguram grotto, Bulguksa temple and Gyeongju Historic Areas are designated as World Heritage Sites by UNESCO. The many major historical sites have helped Gyeongju become one of the most popular tourist destinations in South Korea.

Sponsored by

The Institute of Electronics Engineers of Korea (IEEK), Korea
The Institute of Electronics, Information and Communication Engineers (IEICE), Japan
The Electrical Engineering/ Electronics, Computer, Telecommunications and Information Association, Thailand

Conference Secretariat

Tel: +82-2-571-2724 / Fax: +82-2-571-2721 / E-mail: itc2011@jcinter.co.kr

Iraqi Journal of Applied Physics

Selma M.H. Al-Jawad
Abbas F.S. Al-Shareefi
Abdulhadi K. Judran

School of Applied Sciences,
University of Technology,
Baghdad, IRAQ

Effect of Thickness on Optical and Electrical Properties of ZnO Prepared by CBD

ZnO Thin films were deposited by chemical bath deposition. Structure, optical, and electrical properties of these films were analyzed in order to investigate their dependence on thickness of films. High quality ZnO films with a low resistivity of 1.3 Ω.cm and transparency above 80% were able to be formed for thickness 95.8nm. X-ray diffraction and spectrophotometer are used to investigate the properties of ZnO films.

Keywords: ZnO, CBD, Thin films, optical properties, electrical properties
Received: 2 November 2010, **Revised**: 29 December 2010, **Accepted**: 5 January 2011

1. Introduction

Zinc oxide (ZnO), a transparent film, is very popularly used due to its unique optical and electronic properties in solar cells [1], photo detectors [2], light emitting devices [3], gas sensor elements [4], and surface acoustic wave guides [5]. Different chemical methods such as chemical bath deposition (CBD) [6,7], spray pyrolysis [8], successive ionic layer adsorption and deposition (SILAR) [9], electrodeposition [10,11], chemical vapor deposition, vapor phase epitaxy, molecular beam epitaxy, RF sputtering, and pulsed laser deposition (PLD) [12] etc. have been used to obtain ZnO films. Compared with the technologically demanding vapor deposition techniques, the deposition of ZnO film from aqueous solution represents a simple and effective route. In addition, the solution growth technology is suitable to obtain stoichiometrical ZnO film because of its oxygen-rich deposition environment, which may be beneficial to the suppression of deeplevel related luminescence and the enhancement of UV emission. Among several solution growth technologies, SILAR and CBD are two methods widely used to prepare ZnO layer from aqueous solution[13]. In SILAR method, a thin layer of precursor ions is adsorbed on the substrate first, and the solid film is formed via the chemical reaction between adsorbed ions and precursor ions with opposite charge. The features of SILAR include the layer-by-layer growing mode and the separate precursor of anionic and cationic solutions, which makes the control over the deposition process fairly convenient. However, the very slow growth rate and the great difficulties involved in the deposition of oxide films have greatly limited its application [14]. Therefore, it is meaningful to develop novel solution techniques for the deposition of high quality semiconductor films in higher growth rate [15] The CBD method is based on the controlled precipitation of objective material, i.e., the heterogeneous precipitation on substrate. However, the bulk precipitation in precursor solution (i.e., the homogeneous precipitation) is inevitable, which will definitely impair the quality of obtained film. Also, the presence of both anions and cations in one reaction vessel makes it difficult to control the film deposition process precisely. Therefore, the development of novel solution growth techniques with higher deposition rate and higher film quality is greatly stressed [14].

2. Experimental details

2.1 Substrate Preparation

Substrate used for deposition ZnO is microscope glass slides, which were first cleaned in distilled water in order to remove the impurities and residuals from their surfaces, followed by rinsing in chromic acid (for one day), to introduce functional groups called nucleation and/or epitaxial centers, which formed the basis for the thin films growth.

2.2. Film preparation

Films were deposited on glass slides by, 10ml of 0.1M ($ZnSO_4$), 10ml of 1M (NH_3) solution. Substrates were then immersed in a beaker containing the reaction mixture for (10-20) min. The beaker was placed in a water bath at temperature (80 ± 5°C). The solution was stirred with a magnetic stirrer as illustrated in Figure (1). And, it was heated with continuous stirring to the required temperature of deposition. Substrates were then taken out after a suitable time, they were washed with distilled water to remove the porous zinc oxide overlayer.

3. Measurements

For the measurements the deposited film from one slide was removed carefully using HCL solution.

3. 1 Thickness Measurement

Zinc oxide thickness was measured by using an optical interferometer method employing He-Ne laser (632nm) with incident angle 45°. This method depends on the interference of the laser beam reflected from thin film surface and then substrate the films thickness was determined using the following formula [16]

$$d = \frac{\Delta x}{x} \cdot \frac{\lambda}{2} \qquad (1)$$

where x is the fringe width, Δx is the distance between two fringes and λ is the wavelength of laser light.

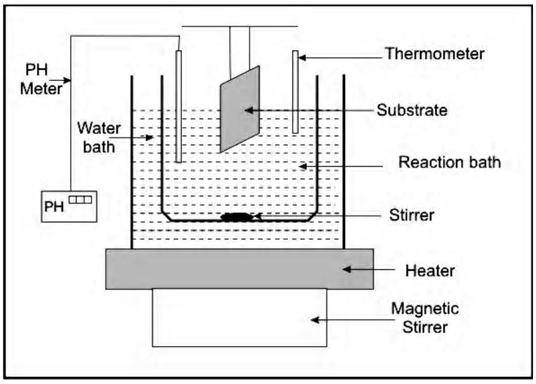

Fig. (1) Experimental arrangement for the deposition of ZnO films

3.2 Structure measurements

The structure analysis films were carried out by analyzing the x-ray diffraction patterns. X-ray diffraction system (Lab XRD-6000/Shimadzu) has the following characteristics:

Source: radiation of CuKα with 1.54Å wavelength,
Scanning speed: (5degree/min),
Incidence angle: 10-60 degree,

The average grain size (GS) of the polycrystalline material can be calculated from the X – ray spectrum by means of Full Width at Half Maximum (FWHM) method (Scherer relation) [17].

$$GS = \frac{A\lambda}{\Delta\theta \cos\theta} \qquad (2)$$

where $\Delta\theta$ is the full-width at half maximum of the XRD peak appearing at the diffraction angle θ, A the shape factor, the value of which depends on the crystalline shape, and generally it is 1

3.2. Optical measurements

Optical measurements were included transmittance and absorption spectra in the wavelength range 300-1100nm using phoenix-2000UV-VIS spectrophotometer .The value of absorption coefficient (α) has been calculated by using the following relation [18,19]:

$$\alpha = 2.303\frac{A}{d} \qquad (3)$$

where A is absorption and d is the thickness of the thin film

The extinction coefficient (K) was calculated using the following equation [20]:

$$K = \frac{\alpha\lambda}{4\pi} \qquad (4)$$

The absorption coefficient (α) and optical band gap (Eg) are related by [21]

$$\alpha h\nu = A(h\nu - Eg)^n \qquad (5)$$

where A is constant depending on transition, h is plank's constant, ν is the frequency of the incident photon, E_g is the optical band gap of the material and n has different values depending on the nature of the absorption process, and equal to 1/2, 3/2, 2 and 3 for allowed, forbidden of direct and indirect transition, respectively

The plot of $(\alpha h\nu)^2$ versus $(h\nu)$ gives the best result. By extrapolating the liner part down to $(\alpha h\nu=0)$ the value of E_g could be determined.

The reflectivity was determined form the values of transmittance (T) and absorbance (A) using the relation ($R+A+T=1$).

The reflectance can be expressed in terms of optical constants, (n) and (K) as [22] follows

$$R = \frac{(n-1)^2 + K^2}{(n+1)^2 + K^2}$$

or

$$n = \left[\left(\frac{1+R}{1-R}\right)^2 - \left(K^2+1\right)\right]^{1/2} + \frac{1+R}{1-R} \qquad (6)$$

3.3. Electrical measurements

3.3.1. Current-Voltage Measurements

From the curve of current-voltage the resistance (R) could be calculated.

The electrical resistivity of the deposited films was determined using the equation [23]:

$$R = \rho\frac{L}{A} \qquad (7)$$

where ρ is the electrical resistivity of the films, L the distance between electrodes and A the area of the ohmic contacts

3.3.2 Activation Energy

The activation energy has been determined by using the relation [24]

$$R = R_{\circ}\exp\left(E_a / KT\right) \qquad (8)$$

where R in resistivity at temperature (T), R_0 is the resistivity at room temperature, K is the Boltzmann′s constant and E_a is the activation energy

4. Results and discussion

4.1. Growth mechanism of ZnO

The CBD is based on the formation of solid phase from a solution, which involves two steps as nucleation and particle growth. In the nucleation,the clusters of molecules formed undergo rapid decomposition and particles combine to grow up to a certain thickness of the film by heterogeneous reactions at the substrate surface. For zinc ions aqueous solution, when the ion product (IP) of the solution is higher than solubility product (SP), the precipitation $Zn(OH)_2$ occurs. It is commonly accepted that the degree of supersaturation (S), defined as the ratio of ion product to solubility product, is an important parameter to evaluate the precipitation process in aqueous solution. When S is lower than 1, no precipitation is formed in solution. When S is lower than 1, no precipitation is formed in solution. When S is higher than 1 but lower than a critical value Sc, the heterogeneous precipitation occurs on the wall of vessel and substrate, because the value of S is not sufficient to induce nuclei in the bulk solution. When S is higher than Sc, a large quantity of nuclei will be formed in the bulk solution and the homogeneous precipitation occurs. Based on this theory, the deposition of high quality film from aqueous solution is to control the value of S, to induce the heterogeneous precipitation on substrates, and to suppress the homogeneous precipitation in the bulk solution.

In this paper, we have made full use of the thermal decomposition nature of $[Zn(NH_3)_4]^{2+}$ in neutral aqueous solution, which will release ions of Zn^{2+} and OH^- into solution and result in the formation of $Zn(OH)_2$ or ZnO particles. Eqs. (9)–(11) illustrate the chemical reactions related to the process.

A dynamic equilibrium exists in the precursor under the presence of excessive ammonia:

$$Zn(OH)_2 + 4NH_3 . H_2O = [Zn(NH_3)_4]^{2+} + 2OH^- + 4H_2O. \qquad (9)$$

During the reaction process in hot water, $[Zn(NH_3)_4]^{2+}$ complex decomposes and $Zn(OH)_2$ precipitation forms:

$$[Zn(NH_3)_4]^{2+} + 4H_2O = Zn(OH)_2(s) + 4NH_4^+ + 2OH^- \qquad (10)$$

As-deposited $Zn(OH)_2$ will transform to ZnO in aqueous solution at the temperature of over 50°C [15]:

$$Zn(OH)_2(s) = ZnO(s) + H_2O \qquad (11)$$

During the chemical reaction process in hot water, with the elapse of the time starting from the initial immersion of substrate in water, three stages will occur subsequently within the liquid film adsorbed on the substrate surface, i.e., the solution stage, the heterogeneous precipitation stage, and the homogeneous precipitation stage. By adjusting the reaction time, the chemical reaction within the liquid film can be terminated in the second stage when the precipitation of $Zn(OH)_2$ occurs on the substrate. Thus, the homogeneous precipitation and the corresponding ''ostwald'' ripening process may be prevented. Then, after a series of successive deposition cycles, ZnO film with certain thickness and high quality will be produced.

4.2. Effect thickness

ZnO will be deposited if the **I**onic **P**roduct (IP) of (Zn^{2+}) and (OH^-) exceed the **S**olubility **P**roduct (SP) of (ZnO). Figure (2) shows the growth kinetics of (ZnO) films with time of deposition at 80°C.

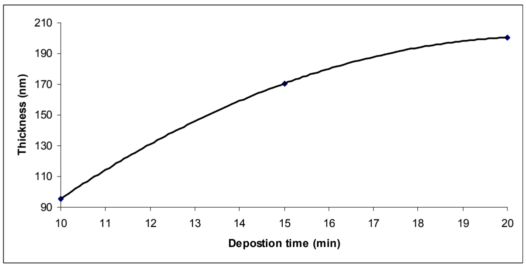

Fig. (2) Variation of film thickness of ZnO film with deposition time

The film thickness increases linearly with time initially but saturates after some time at some terminated thickness. In the initial stages of growth, the thickness increases at a fast rate. Then the rate decreases resulting in a terminal thickness. The saturation behavior of the film thickness is because of eventual reduction in the ionic product of (ZnO) in the solution to values about the solubility product and coagulation of colloidal particles of (ZnO) to form larger particles which cannot be adsorbed.

4.3. Structure properties

The results of our structural studies of the ZnO films were done with x-ray diffraction (XRD) and show (100), (002), and (101) distinct diffraction peaks for the films grown in this study, as shown in Fig. (3).

The average grain size was calculated using Scherer's formula (1), the values of average increases with thickness of films, as shown in Fig. (4). Increasing of grain size may be due to the combined effect of increase in Zn incorporation, increase in growth rate and reorientation effect.

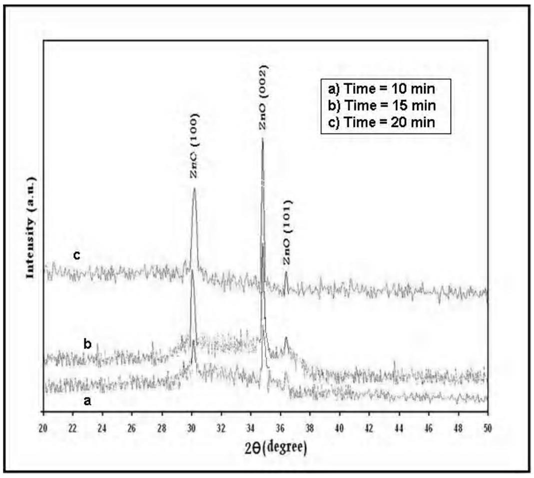

Fig. (3) X-ray diffraction of ZnO films for different thicknesses

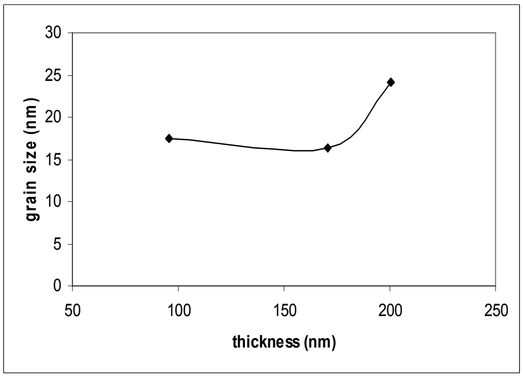

Fig. (4) Variation average grain size with thickness

4.4 Optical Properties

Transmission spectra depend on the chemical and crystal structure of the films, and also on the film thickness and on films surface morphology. The effect of thickness films on these spectra is shown in Fig. (5a). Films transmission decreases with increasing thickness of the films because of an increase of grain size as a result of increasing the films thickness and consequence transmission decreases because of an increase of grain size as a result of increasing the film thickness and consequence transmission decreases. While figure (5b) shows be the influence thickness on absorbance. The absorbance increased with increasing in thickness of the films, this is due to the increasing in the thickness of deposited films. The data from transmission spectrum are used to calculate absorption coefficient by using Eq. (3). The effect of thickness films on reflectance spectra is shown in Fig. (5c).

The absorption coefficient decreases with increasing the deposition time and this attributed to the effect of the thickness. The energy gap (E_g) value is calculated by extrapolation of the straight line of the plot of $(\alpha h\nu)^2$ versus photon energy for thickness as shown in Fig. (7).

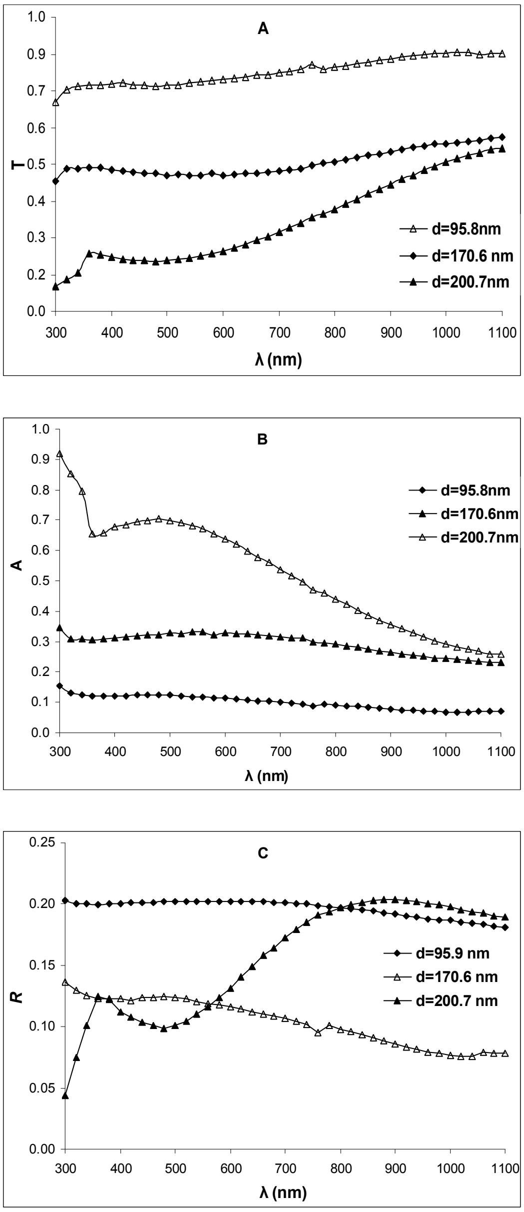

Fig. (5) transmittance (T), absorbance (A), and reflectance (R) as function of wavelength under different thicknesses

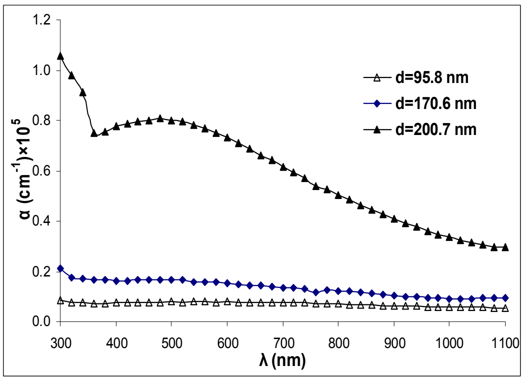

Fig. (6) variation of absorption coefficient (α) as function of wavelength for different thicknesses

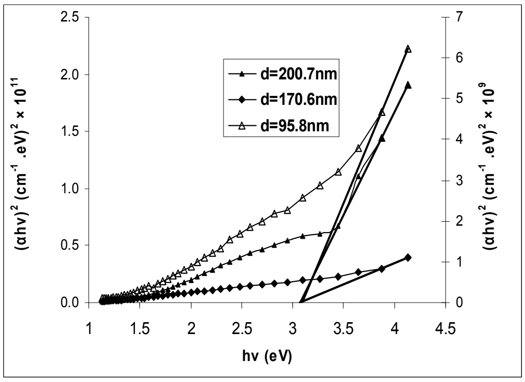

Fig. (7) variation of absorption coefficient (α) as function of wavelength for different thicknesses

The linear dependence of $(\alpha h\nu)^2$ with $(h\nu)$ indicates direct band gap. It is clear from Fig. (7) that the direct energy gap value is constant for different thicknesses and equal 3.27eV and These results are consistent with other published results such as results of Y. Kwon et al [25]. Variation of the extinction coefficient with wavelength is shown in Fig. (8) for different thicknesses shows a steep relationship indicating sharp increase in the absorption with increasing wavelength and.

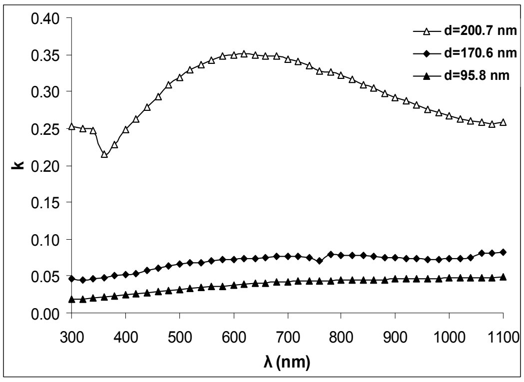

Fig. (8) variation of the extinction coefficient (K) for function of wavelength for different thicknesses.

Studying the refractive index will complete the fundamental study of the optical properties and optical behavior of the material. Figure (9) shows the variation of refraction index of ZnO with wavelength and .These results are consistent with other published results such as results of Al-Shareefi [26].

4.6 Electrical properties

Electrical resistivity measurement was done on the samples and was found to be increasing with increase thickness. Figure (10) depicts the variation of resistivity with thickness, it is clear that resistivity increases with thickness is noticed. More probably the increasing in resistivity is due to change in average grain size which we have already studied These results are consistent with other published results such as results of Al-Jawad et al. [27].

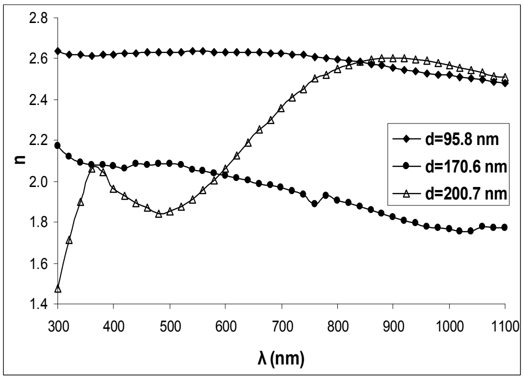

Fig. (9) variation of the refractive index (n) as function of wavelength for different thicknesses

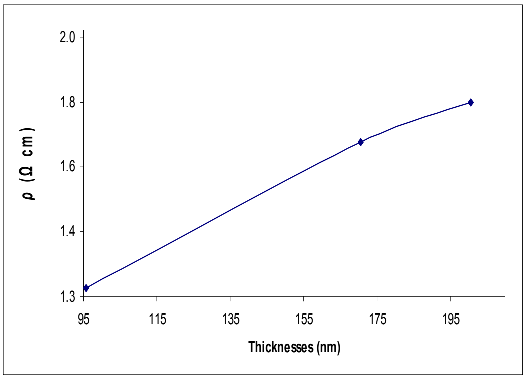

Fig. (10) Variation in resistivity with thicknesses

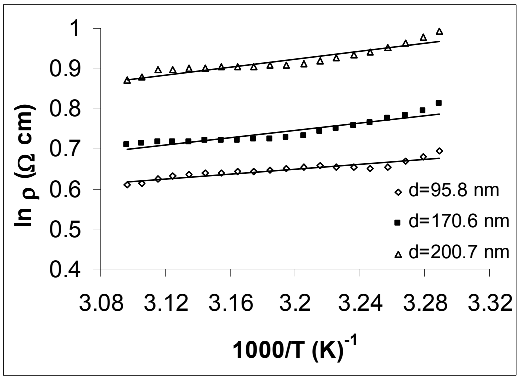

Fig. (11) The relationship between resistivity and temperature for ZnO films

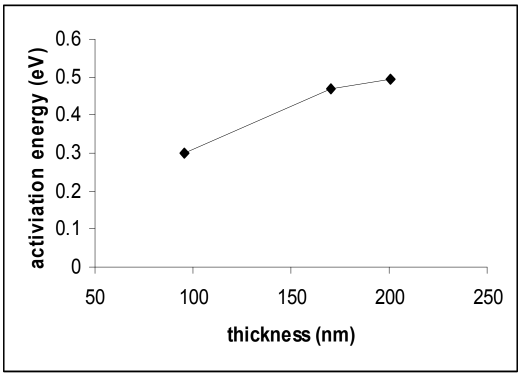

Fig. (12) Activation energy as a function of thickness

Figure (11) shows the relationship between lnρ and 1000/T for ZnO films, from which we calculate the activation energy E_a using Eq. (8). The activation energy depends on the thickness and it will be increasing with increasing thickness as illustrated in Fig. (12).

5. Conclusion

Zinc oxide thin films have been deposited by CBD on glass substrates. The electrical, structure, and optical properties of these films were investigated as a function of the thickness. Electrical resistivity decreasing with decreasing thickness, optical transmittance was much affected by thickness where it increasing with decreasing thickness.

References

[1] K. Keis et al., *Sol. Energy* 73 (2002) 51.

[2] S. Liang et al., *J. Cryst. Growth* 225 (2001) 110.

[3] N. Saito et al., *Adv. Mater.* 14 (2002) 418.

[4] Pizzini et al., *J. Electrochem. Soc.* 136 (1989) 1945.

[5] F.C.M. Van de Pol, *Ceram. Bull.* 69 (1990) 1959.

[6] A. Ennaoui et al., *Sol. Energy Mater. Sol. Cells* 54 (1998) 277.

[7] M. Ortega-Lopez et al., *Mater. Res. Bull.* 38 (2003) 1241.

[8] M.L. de la Olvera et al., *Sol. Energy Mater. Sol. Cells* 71 (2002) 61.

[9] A. Jimenez-Gonzalez, R. Suarez-Parra, *J. Cryst. Growth* 167(1996) 649.

[10] P.M. Izaki, T. Omi, *J. Electrochem. Soc.* 144 (1997) 1949.

[11] D. Gal et al., *Thin Solid Films*, 361/362 (2000) 79.

[12] T.H. Kim et al., *Appl. Surface Sci.*, 255 (2009) 5264–5266.

[13] X.D. Gao, X.M. Li, W.D. Yu, *Mater. Res. Bull.* 40 (2005) 1104–1111.

[14] T.P. Niesen, M.R.D. Guire, *Solid State Ionics* 151 (2002) 61.

[15] X.D. Gao_, X.M. Li, W.D. Yu, *Solid State Chem* 177 (2004) 3830–3834.

[16] P.K. Nair et al., *J. of Phys. D: Appl. Phys.*, 24 (1991) 441.

[17]. B.D. Cullity and S.R. S tock, **"Elements of X-Ray Diffraction"**, 3rd ed., Prentice-Hall (U.S.A) 2001.

[18] T. Yamamoto et al., *J. of Chem. Mater.* 4 (1992) 570 .

[19] S. Bini et al., *J. of Energy* 20 (2000) 405.

[20] S.M. Sze and K.K. Ng **"Physics of Semiconductor Devices"**, 3rd ed., John-Wiley and Sons (2007).

[21] A. Galdikas et al., *J. Sensors and Actuators* B 67 (2000) 76.

[22] K.L. Chopra, **"Thin Film Phenomena"**, McGraw-Hill Co. (1969).

[23] J.J. Loferski et al., *Erciyes Universitesi Fen Bilimleri Enstitusu D ergisi*, 19 (1-2) (2003) 96

[24] H. Metin and R. Esen, *Erciyes Universitesi Fen Bilimleri Enstitusu D ergisi*, 19 (1-2) (2003) 102

[25] Y. Kwon et al., *Appl. Phys. Lett.* 84 (2004) 14.

[26] A.F. Al-Shareefi, "Deposition and Study of Physical Properties of Cu_xS Thin Films Prepared by Chemical Bath Deposition", M.Sc. thesis, University of Technology, Baghdad (2008).

[27] S.M. Al-Jawad, "Study of Some Physical Properties of CdS Films Prepared by Chemical Bath Deposition", Ph.D. thesis, University of Technology, Baghdad (2006).

Iraqi Journal of Applied Physics

Yassin A. El-Gendy[1]
Magdy Hamam[1]
Nagy H. Teleb[2]
Ali M. Salem[2]
Munir S. Selim[2]

[1]*Faculty of Science, Helwan University, Cairo, Egypt*
[2]*Electron Microscope and Thin films Department, Physics Division, National Research Centre, Cairo, Egypt*

Effects of Temperature on The Properties of Amorphous-to-Crystalline Transition in $AgSbSe_2$ Thin Films

Nearly stoichiometric thin films of the ternary $AgSbSe_2$ compound have been deposited at room temperature by conventional thermal evaporation of the presynthesized material onto glass substrate. The X-ray and electron diffraction studies revealed that the as-deposited films are amorphous in nature, while an amorphous-to-crystalline phase transition could be obtained by thermal annealing at 373 K. The elemental chemical composition of as-deposited films was confirmed using the energy dispersive X-ray analysis. The transmission spectra of the as-deposited and annealed films were recorded at normal light incidence in the wavelength range 600-2500 nm. The refractive index and optical band gap have been calculated for the investigated films. The dispersion parameters, (E_o, E_d) static refractive index $n_s(0)$, static dielectric constant, ε_s and the carrier concentration to the effective mass ratio, N/m^* have been calculated. An analysis of the optical absorption spectra revealed anon direct optical transition characterizing the as-deposited films and those annealed at 343 and 374 K while; direct and indirect optical transitions characterized the films annealed at 398 K

Keywords: $AgSbSe_2$, Thin films, Electron diffraction, Amorphous-crystalline transition
Received: 22 Novembder 2010, **Revised**: 29 January 2011, **Accepted**: 5 February 2011

1. Introduction

Due to extensive applications in solid-state devices and future prospects, chalcogenide glasses have received much attention in recent years. A good device is one that is of low cost, fast, accurate and easy to use. Amorphous selenium has been emerged as promising material because of its potential technological importance. It is widely preferred in the fabrication of electrophotographic devices and, more recently, switching and memory devices [1, 2] have found selenium-based materials to offer attractive advantages. The use of chalcogenide films for reversible optical recording by the amorphous-to-crystalline phase change has recently been reported [3].

Silver-containing chalcogenide glasses are considerable interest for applications in optical recording and as solid electrolytes. Therefore, the knowledge of optical, electrical, and structural properties of Ag-chalcogenide amorphous materials is of essential importance. The $AgSbTe_2$ [4], $AgSbS_2$ [5], and $AgInSbSe_2$ [6] systems have been previously studied, however, very little work concerning the optical and electrical properties of $AgSbSe_2$ have been presented [7-9]. In the present work, a systematic study of the structure and optical properties of thermally evaporated $AgSbSe_2$ thin films annealed at different temperatures has been studied. The effect of thermal annealing on the refractive index, high frequency dielectric constant (ε_∞), and carrier concentration to the effective mass ratio (N/m^*) were presented.

2. Experimental details

Polycrystalline ingot of the ternary $AgSbSe_2$ compound was prepared by the direct fusion of a mixture of the constituent elements in stoichiometric ratio, and purity 99.999%, in vacuum-sealed silica tube. Thin films were deposited by conventional thermal evaporation of the presynthesized material onto precleaned glass substrates held at room temperature, in $\sim 1.5\times 10^{-3}$Pa vacuum using a high vacuum coating unite (Type Edwards 306A). The structural characteristics of the prepared ingot material as well as the as-deposited and annealed $AgSbSe_2$ films were examined by means of an X-ray diffractometer (Type Philips X'pert) with Ni-filtered CuK_α radiation operating at 35kV and 100 mA. The chemical composition of the as-deposited films was identified using energy dispersive X-ray unit interfaced with a scanning electron microscope (Type JEOL-JSGM-T200). The microstructure of the as-deposited and annealed films was also examined using Transmission electron microscope (Type JEOL-JSGM-T1230). Double beam spectrophotometer, with automatic computer data acquisition (Type Jasco, V-570, Rerll-00, and UV–VIS–NIR), photometric accuracy of ±0.002–0.004

absorbance and ±0.3% transmittance, was employed at normal light incidence to record the optical transmission and reflection spectra of the asdeposited and annealed films over the wavelength range 600–2500 nm. The thickness of the deposited films was from the interference fringes [10].

3. Results and discussions

3.1 Structural characterization

The X-ray diffractgrams of the prepared $AgSbSe_2$ bulk material as well as the films annealed at different annealing temperatures, T_a are shown in Fig. (1). Comparing the reflection planes of Fig. (1a) with the standard XRD data (JCPDS cards no 12-0379), indicates that all the reflection planes can be indexed to the cubic phase of the ternary compound $AgSbSe_2$ with a cell parameter a=0.578nm. No reflections corresponding to any of the free elements or binary alloys were observed.

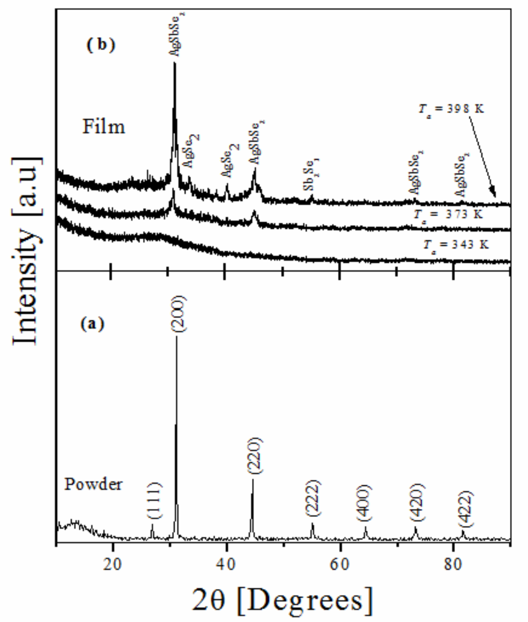

Fig. (1) X-ray diffraction pattern of (a) the prepared $AgSbSe_2$ powder and (b) annealed films (of thickness 780 nm)

The XRD analysis, carried out on the as-deposited films (not given) and those annealed for 1 hour in an Ar atmosphere at annealing temperatures T_a<343 K are amorphous in nature, while those annealed at T_a≥373 K are crystalline. Analysis the XRD diffraction pattern of the films annealed at T_a≥373 K indicates that the film contains two peaks at 2θ=30.97° and 44.39°, respectively, corresponding to reflections from (200), (220) planes of $AgSbSe_2$ single cubic phase. However, the XRD pattern for the film annealed at 398 K shows small diffraction peaks at 2θ=33.52°, 40.41° and 55.05°, respectively, corresponding to reflection from the (112), (122), and (514) planes, which belongs to the binary Ag_2Se, Sb_2Se_3 phases, beside $AgSbSe_2$ as a major phase.

Transmission electron micrographs of as-deposited $AgSbSe_2$ films, and those annealed at T_a≤343 K showed no discernible structure (See Fig. 2). The corresponding diffraction patterns exhibited diffuse rings confirming the amorphous nature of the films as revealed by X-ray diffraction. On the films beinge annealed at T_a≥373 K, a distinct structure was observed in the transmission mode. The corresponding selected area diffraction shows crystallization of the films, as identified previously via X-ray diffraction analysis.

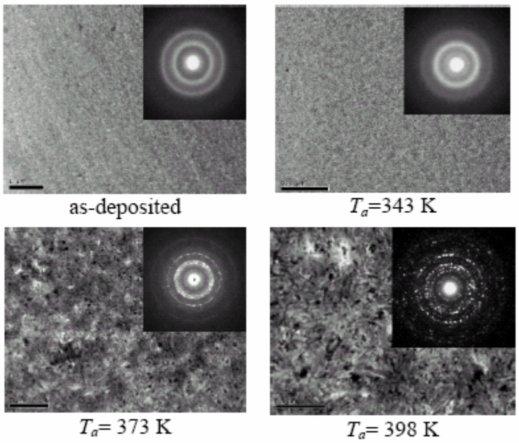
as-deposited T_a=343 K

T_a= 373 K T_a= 398 K

Fig. (2) TEM micrograph and the corresponding electron diffraction pattern of the annealed $AgSbSe_2$ film. Film thickness 70 nm

Figure (3) shows the EDX spectra for a typical representative sample of $AgSbSe_2$ films deposited onto glass substrate.

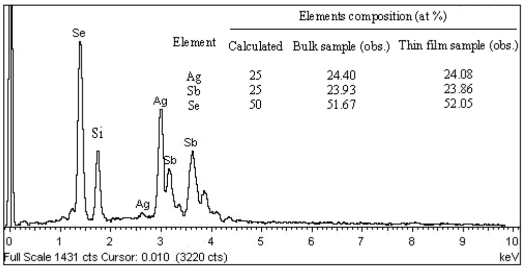

Element	Elements composition (at %)		
	Calculated	Bulk sample (obs.)	Thin film sample (obs.)
Ag	25	24.40	24.08
Sb	25	23.93	23.86
Se	50	51.67	52.05

Fig. (3) EDX spectra of $AgSbSe_2$ film deposited onto glass substrate. Film thickness 780 nm

The result indicates that the chemical composition of $AgSbSe_2$ films had elemental composition of 24.08:23.86:52.05 corresponding to Ag: Sb: Se, which indicating a deficiency in Ag (~0.92 at%) and Sb (~1.14 at%) with an excess of Se (~2.05 at%) hence, led to consider that the as-deposited film had a chemical formula $Ag_{0.963}Sb_{0.954}Se_{2.082}$, revealing a nearly stoichiometric composition. A comparison between the elemental chemical compositions of the prepared bulk material, as-deposited films, and the calculated values are shown in the inset of Fig. (3).

3.2 Optical properties of AgSbSe2 films

Figure (4) shows the transmission spectra of asdeposited AgSbSe $_2$ film of thickness 780 nm and another samples of the same film thickness annealed in Ar atmosphere for 1h, at annealing temperatures 343, 373 and 398 K. It was found that the absorption edge shifts towards lower energies as the annealing temperatures increases. Furthermore, the transmission was found to decrease with the increasing in the annealing temperatures.

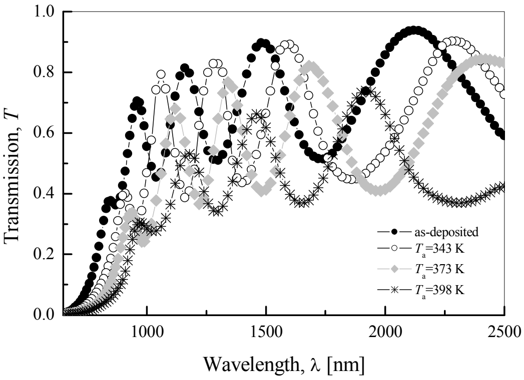

Fig. (4) Transmission spectra of $AgSbSe_2$ thin films annealed at different temperatures

The refractive index, *n*, film thickness and the order of interference of the investigated films were computed from the transmission spectra using the well-known Swanepole method [10] with s=1.51 (substrate refractive index). The sets of values of refractive index calculated according to the above mentioned method can be fitted to a reasonable function such as the two-term Cauchy dispersion relationship; $n(\lambda)=a+b/\lambda^2$; (where *a* and *b* are the Cauchy parameters) which can be used for extrapolation the refractive index to shorter wavelengths. The refractive indexes, *n* of $AgSbSe_2$ films annealed at different temperatures are shown in Fig. (5).

As could be seen from the figure, the refractive index decreases with increasing wavelength and increases on increasing the annealing temperature. Wemple and DiDomenico [11] have developed a model where the refractive index dispersion is studied in the region of transparency below the gap, using the single-effective oscillator approximation. Defining two parameters, the oscillator energy, E_o and the dispersion energy E_d this model concludes that:

$$n^2 = 1 + \frac{E_o E_d}{E_o^2 - E^2} \qquad (1)$$

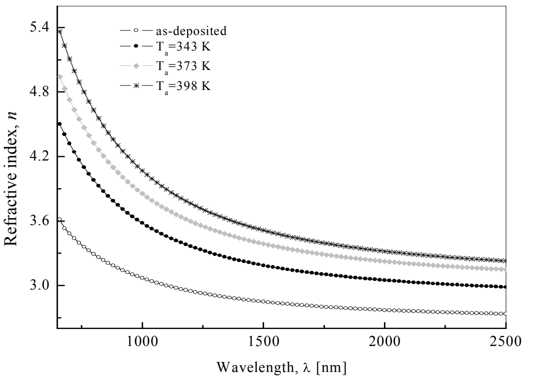

Fig. (5) spectral distribution of refractive index, n for as-deposited and annealed $AgSbSe_2$ films

Both Wemple parameters can be obtained from the slope and intercept of the plot $(n^2-1)^{-1} = f(E^2)$ with the y-axis as shown in Fig. (6).

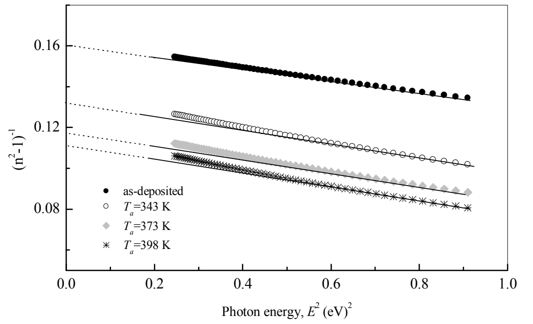

Fig. (6) plot of $(n^2-1)^{-1}$ vs. photon energy

The values of Wemple-DiDomenico dispersion parameters, E_o, E_d static refractive index, no (calculated extrapolating the Wemple-DiDomenico optical-dispersion equation to, $E\rightarrow\infty$; (n_o= $1+E_d/E_o$) as well as static dielectric constant, ε_s for the $AgSbSe_2$ films annealed at different temperatures are listed in Table 1. The oscillator energy E_o is related by an empirical formula to the optical gap value: $E_o \approx 2E_g$ [11]. The calculated values of the optical band gap are also presented in Table1.

Table (1) Refractive index dispersion parameters

T_a (K)	E_d (eV)	E_0 (eV)	n_0	ε_s	$E_o/2\approx E_g$ (eV)	$E_g^{ind.}$ (eV)
303	13.673	2.204	2.684	7.202	1.102	1.160
343	13.923	1.885	2.896	8.386	0.943	1.081
373	14.632	1.766	3.047	9.285	0.882	0.966
398	14.907	1.716	3.112	9.687	0.851	0.930

The obtained refractive index data can be further analyzed to obtain the high frequency dielectric constant via a procedure that describes the contribution of the free carriers and lattice vibration modes of the dispersion. The optical dielectric constant of AgSbSe2 films was calculated using the relation [12].

$$\varepsilon^{\bullet} = \varepsilon_1 + i\varepsilon_2 = (\varepsilon_1^2 + \varepsilon_2^2)^{1/2} \qquad (2)$$

where ε_1 and ε_2 are the real and imaginary parts of the dielectric constant. The values of ε_1 and ε_2 for different incident photon energies can be obtained from the values of n and k ($k = \alpha\lambda/4\pi$) using the well-known relations:

$$\varepsilon_1 = n^2 - k^2, \varepsilon_2 = 2nk \qquad (3)$$

Since the reflectivity of a semiconductor in the NIR region shows anomalous dispersion as the incident photon energy approaches the corresponding value of plasma wavelength, λ_p. When $n^2 >> k^2$ and $\omega\tau << 1$. The real dielectric constant can be expressed as [13]:

$$\varepsilon_1 = \varepsilon_L - [(\varepsilon_L \omega_p^2 / \omega^2)] \qquad (4)$$

$$\omega_p^2 = \frac{e^2 . N/m^{\bullet}}{\varepsilon_o}$$

where ε_L is the lattice dielectric constant (or limiting value of the high frequency dielectric constant), ω_p the plasma frequency and ω is the angular frequency (=2πc/λ, c is the speed of light) of the lattice atoms, e is the electronic charge, N/m^* carrier concentration to the effective mass ratio, and ε_o is the dielectric permittivity 8.85×10^{-12} F/m. Therefore, plotting ε_1 vs. ω^{-2} in the NIR spectral region (not shown) allow us to determine the values of the plasma frequency, ω_p and lattice dielectric constant, ε_L from the slope and intercept, respectively. These calculated values are listed in Table (2). The observed disagreement between the values of static dielectric constant obtained according to Wemple and DiDomenico single-effective oscillator model and lattice dielectric constant obtained according to Eq.3 may be attributed to the contribution of the free carriers to the refractive index [14].

Table (2) values of ε_L, n , ω_p and N/m*

T_a (K)	ε_L	$n=(\varepsilon_l)^{1/2}$	ω_p ($\times10^{-15}$ s^{-1})	N/m* ($\times10^{22}$.cm^{-3})
303	7.983	2.825	4.39	1.04
373	9.694	3.157	7.51	1.48
398	11.009	3.318	9.19	1.66
423	11.464	3.386	9.46	1.73

The analysis of the absorption coefficient, α at the fundament absorption edge was found to follow the relation;

$$(\alpha\hbar\nu) = A \times (\hbar\nu - E_g)^p \qquad (5)$$

where A is constant and the exponent p characterize the type of the optical transition. A plot of $(\alpha h\nu)^{1/2}$ for as-deposited film and for those annealed at 343 and 378 K (shown in Fig. 8a) indicates a non direct optical transition with energy values 1.16, 1.08 and 0.97 eV, respectively. However, the analysis of the absorption coefficient for the film annealed at 398 K (Fig. 8b) indicated the presence of both direct and indirect optical transition with values of 0.96 and 0.93 eV, respectively.

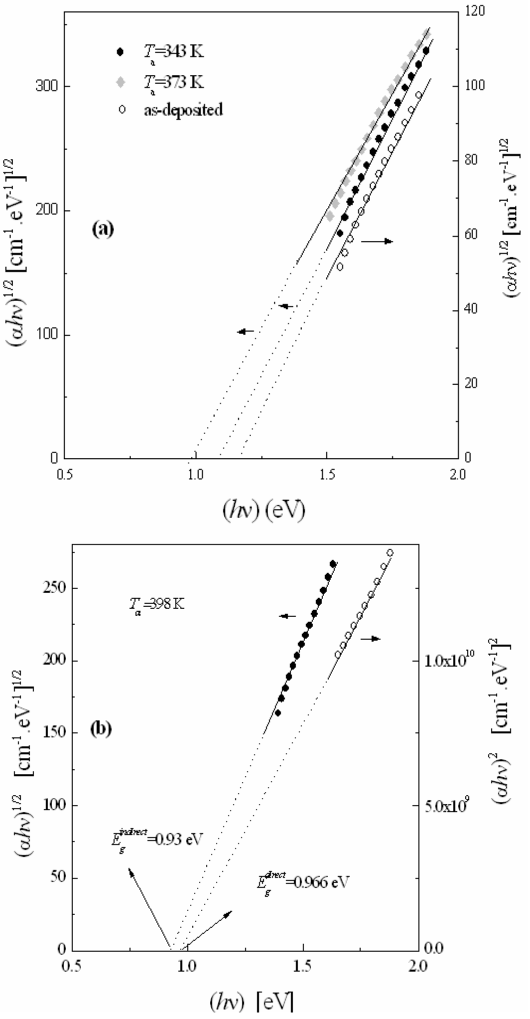

Fig. 7 a, b (a) plot of $(\alpha h\nu)^{1/2}$ for the as-deposited film and those annealed at 343 and 373 K vs. photon energy; and (b) plot of $(\alpha h\nu)^2$ and $(\alpha h\nu)^{1/2}$ for the film annealed at 398 K vs photon energy.

4. Conclusion

Nearly stoichiometric $AgSbSe_2$ thin films were deposited at room temperature by thermal evaporation onto glass substrates. The X-ray and electron diffraction studied revealed that the as-deposited films and those annealed at temperatures <373K are amorphous in nature, while an amorphous-to-crystalline phase transtion could be obtained for the films annealed at temperatures ≥373K. Onset of mainor peaks corresponding to Ag_2Se and Sb_2Se_3 binary phases, beside the ternary $AgSbSe_2$ as a major phase were obtained when the film being annealed at 398K. The effect of annealing temperature on the refractive index, high frequency dielectric constant (ε_∞), and carrier concentration to the effective mass ratio (N/m^*)

were presented. The refractive index and consquently the high frequency dielectric constant were found to increase with the increase in the annealing temperatures. The analysis of the optical absorption coefficient for the deposited films reveald the presence of a non direct optical transition for as-deposited and those annealed at 343 and 373 K, while a direct and non direc optical transition for the film annealed at 398 K.

References

[1] N. Pandey et al., *Chalcog. Lett.*, 2 (2005) 39.
[2] M.A. Afifi et al., *J. Mat. Sci.*, 41 (2006) 7969.
[3] M. Luo and M. Wuttig, *Adv. Mater.*, 16 (2004) 439.
[4] R. Detemple et al., *Appl. Phys. Lett.* 83 (2003) 2572.
[5] J. Gutwirth et al., *J. Non-Cryst. Solids*, 354 (2008) 497.
[6] J. Li et al., *Proc. SPIE*, 4085 (2001) 125.
[7] K. Wang et al., *Appl. Phys.*, A81 (2005) 1601.
[8] H. El-Zahed, *Thin Solid Films*, 238 (1994) 104.
[9] H. Soliman, D. Abdel-Hady and E. Ibrahim; *J. Phys.: Condens. Matter*, 10 (1998) 847.
[10] R. Swanepoel, *J. Phys.*, E16 (1983) 1214.
[11] S.H. Wemple and M. Di Domenico, *Phys. Rev.*, B3 (1971) 2767.
[12] N.R. Koteeswara and K.T.R Ramakrishna, *Mater. Res. Bul.*, 41 (2006) 414.
[13] A. Osama, M.M. Abdel-Aziz and I.S. Yahia, *Appl. Surf. Sci.*, 255 (2006) 4829.
[14] M. Parlak, A.F. Qasrawi and C. Ercelebi; *J. Mater. Sci.*, 38 (2003) 1507.

IOP Institute of Physics

Sensors and Their Applications XVI

12-14 September 2011, Clarion Hotel, Cork, Ireland

Organised by the IOP Instrument Science and Technology Group
Co-sponsored by Institute of Physics and Engineering in Medicine (IPEM) and National Physical Laboratory (NPL)

The sixteenth in the series of conferences on Sensors & their Applications (S&A XVI) will be hosted by Tyndall National Institute at University College Cork, Ireland in September 2011. This popular event follows previous conferences in the series that began in Manchester in 1983 and included the first of the highly successful Eurosensors conference at Cambridge in 1987 and at Southampton in 1998.

The S&A series of conferences provides an excellent opportunity to bring together scientists and engineers from academia, research institutes and industrial establishments to present and discuss the latest results in the field of sensors, instrumentation and measurement.

Conference Themes

Papers are invited in the following themes including, but not restricted to:

Technologies:

- Optical Sensors
- Chemical and gas sensors
- Sensors in biology and medicine
- Advances in sensing materials
- Nanotechnology for sensors and actuators
- Smart sensors and interface electronics
- MEMs and Silicon fabrication techiques
- Imaging: integrated actuators
- Thick and thin film sensors
- Sensor modelling
- Sensor packaging and assemblies

Application areas:

- Environmental sensing
- Medical/healthcare/environmental sensing
- Robotic and remote sensing
- Tomography
- Domestic electronics and smart homes
- Crime prevention
- Automotive and aerospace
- Leisure industry and toys
- Food and agriculture
- Marine
- Energy and power

Key dates

- Paper submission deadline extended to: 15 April 2011
- Notification of paper acceptance: 29 April 2011
- Registration deadline: 5 September 2011

Shawkat I. Jubair

Department of Physics,
College of Science,
University of Baghdad,
Baghdad, Iraq

Calculation of Buildup Factors for Ceramic Materials

The aim of this research is to obtain a composite material that can be used for the shielding against gamma rays utilized in many scientific, industrial and medical applications as well as protect the environment and people from the risk of radiation. In other word measured and determine the amount of shielding required to provide personal protection and environmental with lowest costs and appropriate selecting materials to reduce radiation doses in industrial facilities and surrounding areas.

Also in medical field, build up factor contributes to determine the amount of radiation dose reach to tumors tissue. So that the buildup factor for ceramic plates manufactured for this purpose was calculated, by using gamma-ray spectroscopy, and sheets of lead as standard material.

Keywords: Gamma attenuation, Composites, Ceramic, Buildup Factor
Received: 26 January 2011, **Revised**: 24 March 2011, **Accepted**: 31 March 2011

1. Introduction

In response to the requirements of development and industrial progress which is moving toward improving the performance of the product in terms of design, manufacturing and low cost. In the field of radiation protection the shielding materials protected from gamma radiation, such as concrete, lead, requires large blocks and then high costs. So the composite material help to solve the problem of shielding, these composite material have properties of multiple commensurate with many industrial applications. Due to their property, that combines characteristics of two or more by passing the misdeeds of each material, in addition, it has the ability to control their properties, both by the type and ratios of component materials or through the design and methods of manufacture, therefore these materials regarded an important material among different engineering materials.

In principle, one's dose in the vicinity of an external radiation source can be reduced by increasing the distance from the source, by minimizing the time of exposure, and by the use of shielding. Distance is often employed simply and effectively. For example, tongs are used to handle radioactive source in order to minimize the dose to the hands as well as the rest of the body. Limiting the duration of an exposure significantly is not always feasible, because a certain amount of time is usually required to perform a given task. Sometimes, though, practice runs before-hand without the source can reduce exposure times when an actual job is carried out [1].

While distance and time factors can be employed advantageously in external radiation protection, shielding provides a more reliable way of limiting personal exposure by limiting the dose rate. In principle, shielding alone can be used to reduce dose rates to desired levels. In practice, however, the amount of shielding employed will depend on a balancing of practical necessities such as cost and the benefit expected, where ceramic available cheap and friend for environment.

The thickness of the shielding required for attenuated the gamma photons depends on the geometrical arrangement for the source and the detector which is used to detect the shielded beam (I) and the initial beam (I_o) or depend on the buildup factors which are depends on the geometry arranges.

When gamma radiation is incident on a finite thickness of material, there exist some probabilities that the radiation will interact in the material and be attenuated. In some instances a photon may interact by the photoelectric effect, Compton scattering and pair production. Any of the common gamma interaction processes may result in secondary photons that have a finite probability of reaching the dose point of interest - inside or outside the attenuating materials.

The extent to which such secondary photons add to the flounce at the dose point is usually described as build up factors [2].

The buildup factor is defined by the ratio of the total radiation quantity at any point to the radiation quantity of radiation reaching the point without any collision. Many theoretical formula of building up factors were presented for the interpolation at arbitrary thickness of shielding materials. In the formula, the geometrical, progression approximation is well known to produce the buildup factors in the wide energy range of various materials and thickness with good accuracy. [3]

Buildup factors for monoenergetic source in infinite media have been calculated several times for various materials in the past 50 years, [4-7], however, only a few experimental results are known.

Therefore this work presents the buildup factors for (Ceramic and Leads) up to 5 mean free path (mfp) for (0.662 MeV photons) by using experimental work.

2. Theory

When a narrow parallel of photons passes though relatively thin shield, Fig. (1), the relative intensity of monoenergetic photons transmitted without interaction through a shield of thickness is:

$$\frac{I}{I_0} = e^{-\mu x} \qquad (1)$$

where I and I_0 are the shielded and initial beam intensities, respectively, μ is the linear attenuation coefficient (in cm^{-1}), and x is the shield thickness in (cm)

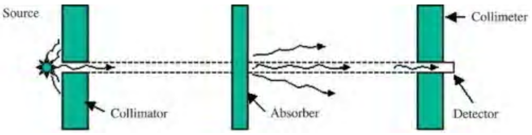

Fig. (1) Measurement of the attenuation of gamma radiation under conditions of good geometry

Ideally, the beam should be well collimated, and the source should be as far away as possible from the detector. The absorber should be midway between the source and the detector, and it should be thin enough so that the likelihood of a second interaction between a photon already scattered by the absorber and the absorber is negligible. In addition, there should be no scattering material in the vicinity of the detector

The linear attenuation coefficient can be considered as the fraction of photons that interact with the shielding medium per centimeter of shielding. It is also known as narrow beam conditions because the source and detector are assumed to be collimated and the measurement made at a short distance [8].

If the incident beam is broad (as shown in Fig. 2), then the measured intensity will be greater than that described by Eq. (1) because scattered photons will also be detected. Such conditions usually apply to the shields required for protection from gamma-ray sources. The increased transmission of photon intensity over the measured in good geometry can be taken into account

$$\frac{I}{I_0} = Be^{-\mu x} \qquad (2)$$

where B is the buildup factor for one energy at the shield thickness x

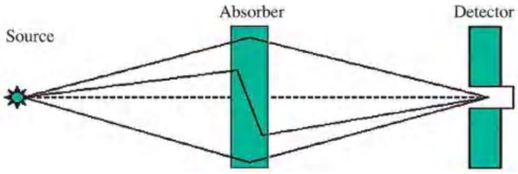

Fig. (2) Gamma radiation attenuation under conditions of broad beam geometry showing the effect of photons scattered into the detector

This formula attempts to estimate the correct number of scattered photons that reach the detector (closest estimate) by using a correction factor to add in the Compton scatter and pair production photons that are ignored by the linear attenuation coefficient formula. Therefore, the value of B can be obtained by dividing Eq. (2) by Eq. (1).

3. Experiment

Figure (3) shows the block diagram for the electronic system which used in this study and its consists of the following units: scintillation detector NaI(Tl) with dimensions 2″×2″, preamplifier (ORTEC) and MCA.

The materials which used as absorbers are blocks from lead material and ceramics slabs. Ceramic slabs made from Iraqi Flint clay consists mainly from alumina and silica, table (1) shows the chemical composition for Flint. The ionic alumina bonds absorbed gamma ray energy more than others bonds.

These slabs were shaped by hydraulic pressing with spherical die, then sintering with temperature by kiln at 1200°C have density (1-1.47) gm/cm^3, thickness (3.1-4.55) mm with diameter (4.1-4.98) cm.

The radioactive source was used in this study is disc shape of Cs-137 which emits gamma photons of 0.662 MeV energy and the activity is 20 μCi.

Table (1) Chemical composition for Flint

Mineral	SiO_2	Al_2O_3	Fe_2O_3	TiO	CaO	MgO	Na_2O	K_2O	L.O.I
Percent	47	34	0.5	2	0.6	0.3	0.46	0.09	15

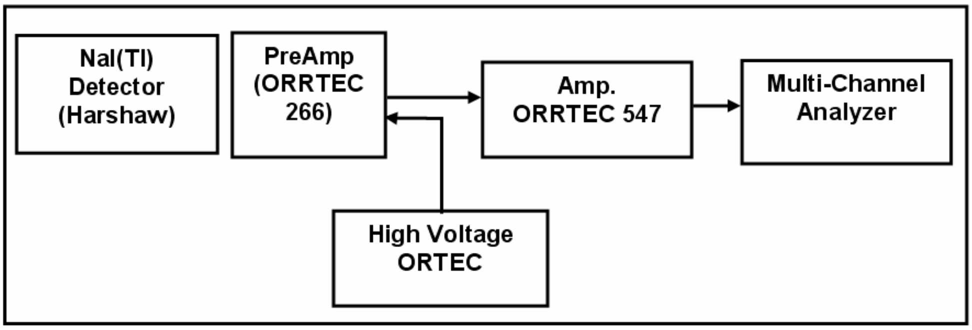

Fig. (3) The block diagram of the Electronic detection system

4. Results and Discussion

In the case of carrying out the shielding calculation for the radiation-shielding ceramic plates, a lead equivalent is generally used. In other words, first, the transmission of lead should be revealed. The data of transmission and build-up factor B of lead and ceramic is described in table (2).

Figures (4) and (5) show the relationship between ln I/I_o versus the thicknesses of slabs of ceramic and lead, from Fig. (4), the linear attenuation coefficient for ceramic was obtained (0.0966 cm^{-1}), and from Fig. (5), the experimental attenuation coefficient for lead was obtained (1.0244 cm^{-1}).

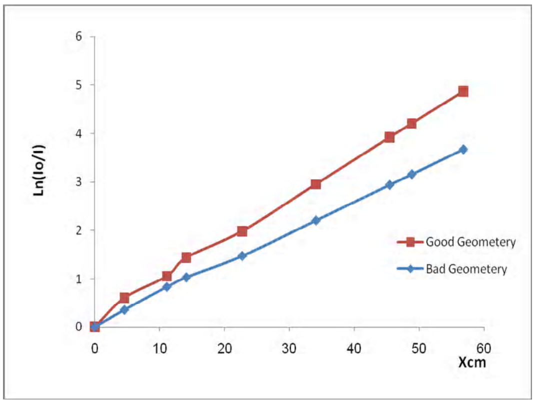

Fig. (4) Logarithm of the intensity versus thickness of ceramic for good and bad geometry

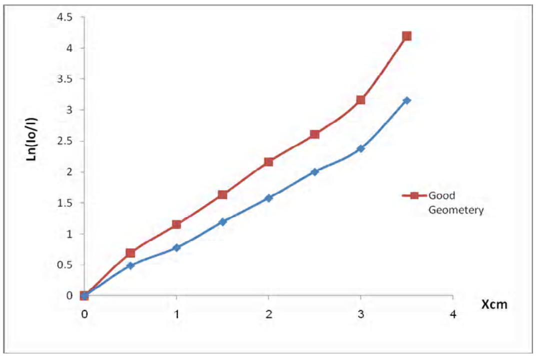

Fig. (5) Logarithm of the intensity versus thickness of lead for good and bad geometry

Table (2) values of mean free path, counts rate per (1000) s, for good and bad geometry and build up factors, for lead and ceramic materials

Lead

μx Experimental	μx Theoretical	N Bad	N Good	Buildup Factor
0	0	53285	5859	1.0000
0.484	0.554	32655	2927	1.2267
0.968	1.109	24404	1859	1.4434
1.452	1.663	16167	1142	1.5566
1.936	2.217	10983	672	1.7970
2.420	2.772	7171	433	1.8210
3.073	3.324	4937	247	2.1980
4.098	4.436	2255	89	2.7840

Ceramic

μx Experimental		N Bad	N Good	Buildup Factor
0		53285	5859	1.0000
0.390		37385	3203	1.2834
0.946		23120	2031	1.2517
1.200		18928	1385	1.5027
1.932		12175	803	1.6666
2.898		5844	305	2.1071
3.864		2805	116	2.6588
4.154		2250	87	2.8436

For comparison between this work and theoretical calculated, the values of theoretical linear attenuation coefficient for lead for 0.662 MeV energy obtained from [7] Fig. (6) (1.108 cm^{-1}). The percentage error ratio of attenuation coefficient for lead is 7.5%.

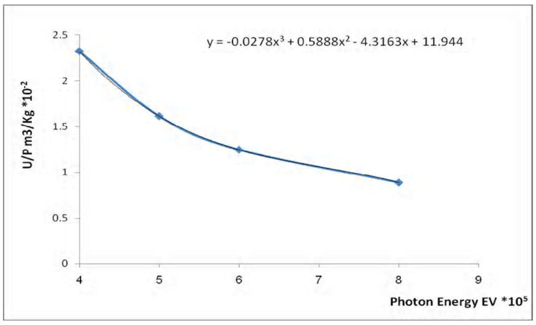

Fig. (6) Mass attenuation coefficients for lead as a function of photon energy [8]

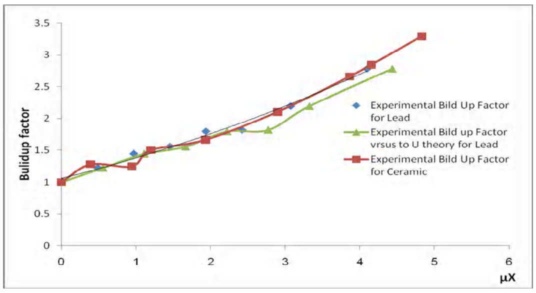

Fig. (7) Buildup factors, B in lead and ceramic as function of the number of relaxation lengths, µx

5. Conclusions

The first object of the present work is to provide a radiation-shielding ceramic capable of ensuring appropriate lightness and easier to dealing with it in radiotherapy, in addition to ensuring sufficient radiation-shielding ability. In other words, it is extremely important that the radiation-shielding means for the therapy ensures sufficient radiation-shielding ability and sufficient relaxability to prevent the body from directly being exposed to gamma rays while a doctor precisely confirm the complexion or the like of the subject

For the shielding performance, a plate thickness at which the transmission of the ceramic and the transmission of lead against a direct ray become equal is represented by a parameter of a lead equivalent. If the gamma ray (direct ray) of the ceramic of 10mm in thickness has a gamma-ray attenuation rate of 50% and lead of 3mm in thickness has a gamma-ray attenuation rate of 50%, then the ceramic of 10mm in thickness has a shielding ability of 3mm Pb (3mm equivalent), Fig.(7).

Therefore the ceramic material can be used as shielding barrier or a shielding protection screen against gamma rays. It is the actual condition that a matter of how to optimize the basic composition of ceramic for properly shielding the gamma rays emitted from the subject and for properly lightness, cheaper, available material and friend of environment to use it in the therapy.

Acknowledgment

Author would like to thank Assistant Professor Asia Al-Mashhadani for her valuable reviewing and remarks on this work.

References

[1] J.E. Turner, **"Atoms, Radiation and Radiation Protection"**, Wiley–VCH Verlag GmbH & Co. KGaA (2007).

[2] M.D. Bethesda, National Council on Radiation Protection and Measurements. Radiation Protection for particle accelerator facilities. NCRP; Report No.144 (2003)

[3] H. Hirayama, *J. Nucl. Sci. Technol.*, 32 (1995) 1207.

[4] M. Mahmoud, *Nucl. Sci. Eng.*, 67 (1978) 341-343 (1978).

[5] H.J. Shian, *Nucl. Sci. Eng.*, 75 (1980) 16-29.

[6] P. Jacob, H.G. Paretzke and J. Wolfel, *Nucl. Sci. Eng.*, 87 (1984) 113-122.

[7] M.M. Chiles, G.W. Allin and J.V. Pace, *IEEE Xplore* (2011).

[8] J.H. Hubbell, *Int. J. Appl. Radiat. Isot.*, 33 (1982) 1269-1290.

Luminescence Characterization of the Bio-Conjugated Quantum Dots with CA125 Antigen Using Linkage Molecules

Lina Zhukov

Institute of Semiconductor Physics,
National Academy of Sciences,
Kiev, Ukraine

Ovarian cancer is the most lethal gynecologic malignancy. This largely reflects the fact that approximately 75% of cases are detected at advanced stages of disease, when cure is unlikely. It is accepted that detecting a greater number of patients with early stage disease by improving screening modalities could significantly improve overall survival. A novel approach to increase the sensitivity and specificity of early detection of cancer is through the application of nanotechnology, where luminescent semiconductor quantum dots (QDs) are conjugated with biomolecules. We report on the luminescence characterization of the bio-conjugated QDs with CA125 antigen using linkage molecules. Kinetic curves of the bio-conjugated 655nm QD luminescence show both photo-enhancement and photo-degradation. Photo-enhancement is measured at various laser density power, temperatures and laser wavelengths. The mechanism of the PL enhancement is discussed.

Keywords: PL spectroscopy, Quantum dots, Cancer biomarkers, CA125 bio-conjugate
Received: 2 December 2010, **Revised**: 5 January 2011, **Accepted**: 12 January 2011

1. Introduction

Ovarian cancer causes more deaths each year among North American women than any other gynecologic cancer. The poor survival rates are largely a reflection of the fact that over 70% of patients are diagnosed with advanced (stage III/IV) disease when 5-year survival rates are less than 20%. This contrasts dramatically with the 80-90% 5-year survival rates associated with patients diagnosed with Stage I or II ovarian cancer. Unfortunately, no good screening tests for ovarian cancer are available. Given our limited understanding of the pathogenesis of epithelial ovarian cancer and consequent difficulty in identifying women at high-risk for development of the disease, there is a great need to establish and translate novel strategies for early detection. Recent discoveries in the molecular biology and molecular genetics of ovarian cancer coupled with technological development in the area of nanotechnology afford an unparalleled opportunity to make radical advances in this arena.

To date, detection of the secreted tumor marker CA125 is the only biomarker available for screening and therapeutic monitoring, however it has limited sensitivity (70%). A novel approach to increase the sensitivity and specificity of early detection of cancer is through the application of nanotechnology, where luminescent semiconductor quantum dots (QDs) are conjugated with biomolecules [2]. Bioconjugation of QDs, i.e. the attachment of specific ligands to them, represents the convolution of biotechnology and nanotechnology yielding hybrid materials, processes and devices. In a case of early cancer detection this approach offers the potential to detect molecules in biological samples at levels below 10^{-7} [3]. We conjugated in this work core-shell CdSe/ZnS luminescence QDs with monoclonal mouse anti- CA125 antibody (AB) as a potential serologic assay. Among different monoclonal antibodies potentially available for CA125 detection, we have selected OC-125 for QD-bioconjugation because it recognizes the defined peptide epitope of the target and can be compared with accepted clinical assays.

Nanometer-scale II-VI compound semiconductors known also as quantum dots (QDs) represent zero-dimensional structures where exciton wave function is confined in three dimensions. This QD’s property creates unique optical charcateristics such as spectral tunable photoluminescence (PL) output with external quantum efficiency in the range of 30 to 50% in surface passivated core-shell compounds [1]. Recent improvements in the synthesis of core-shell QDs with the polymer coating show a promise of their wide applications as bio-luminescence markers [2,3]. Tunable wavelength emission of the luminescence QDs was achieved from a variety of the inorganic semiconductors, predominantly of II-VI compounds such as CdSe, CdTe, CdS, etc. To obtain a noticeable quantum efficiency of the QD luminescence the core-shell structures can be effectively designed in a form of colloidal particles. A successful example represents CdSe/ZnS core/shell coupling, where large band-gap material (ZnS) serve as a surface passivating layer and as a barrier assisting the electron-hole confinement in the CdSe core [4]. A stability and efficiency of the QD luminescence is a critical aspect.

2. Photoluminescence (PL) System

The PL spectroscopy was performed between 80K and room temperature, using a 50mW HeCd laser line at 325 nm or 200mW Ar^+ laser line at 488 nm as the excitation sources. Laser power density varied by use of a set of calibrated neutral density filters and could be focused down to 100 microns spot. At low intensity measurements the laser beam was un-focused with approximately 1.5 mm laser spot diameter at the sample surface. The PL signal was collected by optics, dispersed by a SPEX 500M spectrometer and recorded by a photo multiplier tube coupled with a lock-in amplifier. All system is computer controlled.

2.1 Anitigen Detection

CA125 assay was determined by using the OC125 mouse monoclonal antibody (Mab) (DAKO Cytomation, Carpinteria, CA), as the detector antibody. These Mabs were produced using lymphocytes from a mouse immunized with OVCA 433, a cell line derived from a papillary serous cystadenocarcinoma of the ovary [4]. We also utilized a biotinylated capture antibody, designated as anti-epithelial ovarian carcinomas (Biomeda, San Francisco, CA). This binds mucin-like glycoprotein molecules containing OC125 defined antigen, similar to mouse monoclonal M1 1 clone [5].

The samples, standards and controls and biotinylated capture antibody were incubated in the microtiter streptavidin-coated black plates from Thermo Electron (Milford, MA). The OC125 mouse Mabs were pre-labeled with QDs 655 goat-F(ab')2 anti-mouse IgG conjugate before applying to the bound (captured) antigen in the solid phase well. The molar ratio 6:1 of Fab-QDs 655 to labeled antibody molecule was found sufficient to get strong PL signal from the labeled complex. These experimental findings are consistent with our previous experience in the application of alternative Zenon antibody labeling method for lung cancer biomarkers evaluation [6], in which specific antibodies were directly labeled with isotype specific Fab fragments conjugated with Alexa Fluor dyes (Molecular Probes, Eugene, OR). Following incubation time with QDs- pre-labeled antibodies and washing steps the plates were read according to emission spectra for the tested QD-bioconjugate (see spectra below).

We used as a reference standard the serial dilution of human CA125 antigen of high purity grade (Research Diagnostics, Inc., Flanders, NJ). Control wells either lacked antigen or contained QDs 655-Fab only (without antibody). The plasma samples from cancer patients were assayed using the reference ELISA kit for measurement of CA125 (Biomeda). The reportable (dynamic) range of CA125 detectable by the Biomeda assay is 0 to 500 U/ml, which reflects the physiological range of CA125 in blood. These standards were used to generate a calibration curve, which is depicted as the fitted line (in red) in Fig. (1). Two blood samples with the lowest and highest CA125 levels (blue dots) were then assayed using PL method, in which OC125 mouse Mab was labeled with QDs 655 (described above). These results show strong concordance of QD 655 assay with reference CA125 measurement (see Fig. 2).

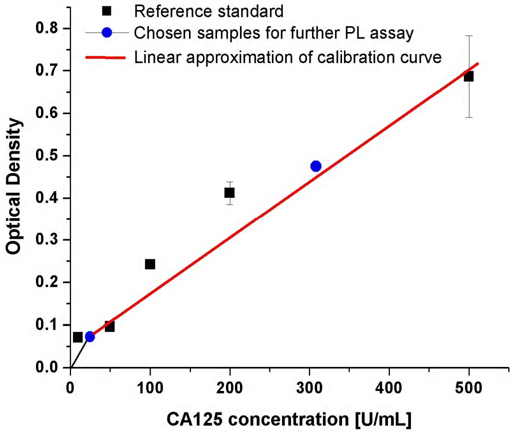

Fig. (1) Concentration of CA125 (U/ml) in cancer plasma samples used in the PL study measured using standard ELISA methodology

3. Results and Discussion

Commercially available CdSe/ZnS polymer coated quantum dots from Quantum Dot Corp. were used [8]. A sample of the Qdot 655 Goat $F(ab')_2$ anti-Mouse IgG conjugate in a form of a mm-size spot was dried on a polished surface of the crystalline silicon substrate to achieve low level of the scattered light. One dried spot contained 2 μl of QD's bio-conjugate diluted with phosphate buffer (PBS) in the 1:50 volume ratio. Bio-conjugated samples contained Qdot 655 $F(ab')_2$ complex fragment conjugated to OC125 detector antibody that recognizes CA125 anti-gene molecule, used in early stage detection of ovarian cancer. Some experiments were done on QD – $F(ab')_2$ – OC125 bio-conjugate structure before attachment to CA125 anti-gene molecule.

(a) Photoluminescence transient [7]

PL spectrum of the CdSe/ZnS quantum dots in the range of 0.73-3.54 eV (350-1700 nm) exhibits only one prominent luminescent band with the maximum at 1.89eV (655 nm) and half-width of 0.09eV at room temperature (Fig. 2).

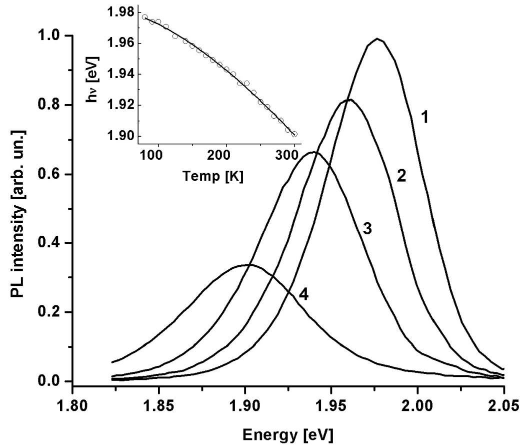

Fig. (2) PL spectrum of the CdSe/ZnS quantum dots in the range of 0.73 to 3.54 eV (350 to 1,700 nm)

When temperature is decreased the PL maximum shows a narrowing and “blue” shift following the temperature band-gap variation of the bulk CdSe, which is described in Fig. (1) by a solid line using Varshni equation.

The following observations were depicted based on the transient PL study.

(1) PL photo-enhancement amplitude can be quite substantial spanning the range from 10% up to 5-fold with respect to the initial luminescence intensity.

(2) The enhancement effect is observed both at 325nm (HeCd) or 488nm (Ar^+) laser excitation. The enhancement rate is increased (time constant reduced) at higher excitation power density as illustrated in (Fig. 3).

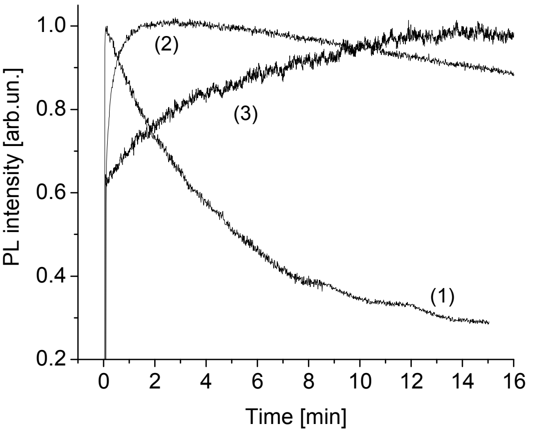

Fig. (3) Photoluminescence spectrum of the CdSe/ZnS quantum dots as a function of time

(3) If the sample subjected to UV exposure was held in dark for definite time, the enhancement effect can be either recovered back which is assigned to reversible enhancement (RE) and the kinetics can be repeated again, or the effect can exhibit non-reversible enhancement (NRE) and show no recovery at room temperatures for at least over night sample storage. Typically RE and NRE occur simultaneously (Fig. 4)

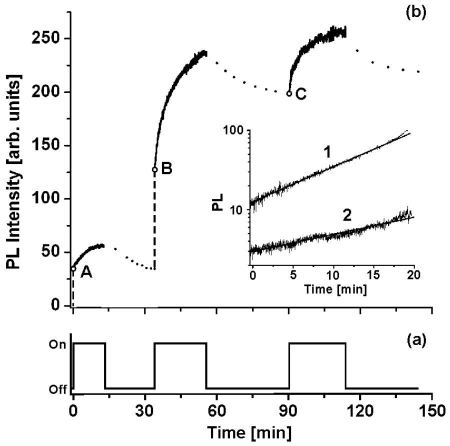

Fig. (4) Photoluminescence spectrum of the CdSe/ZnS quantum dots vs. the time rated signal of excitation

(4) Both RE and NRE kinetics are thermally activated meaning that they are substantially slowed down when temperature decrease. Specifically, the RE time constant (τ_{RE}) yields ten’s of minutes at 300K and its transient kinetics is no longer observed below 240K.

(5) The PL spectrum measured at room temperature before and after enhancement completed shows no noticeable variation of the peak position and the half-width.

(b) Silicon Substrate

With the goal of increasing sensitivity of the screening test for ovarian cancer by detecting low levels of CA125 and in reducing background to zero over a broad spectral range, a Si substrate was used in place of the commercially available plastics used in standard immunosorbent assay.

A Si wafer as a substrate shows negligible scattered signal in a broad visible spectral range from 350 to 725nm, making it ideal for use in quantum dot optical multiplexing. Figure (5) shows the comparison between some common plastics used in ELISA plates compared to Si wafer.

The samples in Fig. (6) were deposited and mapped on Si wafer for better signal/noise ratio. Using a Si surface allows for the detection of very low levels of PSA. Samples were mapped at the 665nm wavelength in the maximum of the QD PL spectrum. In Control 1 total PSA level = 2.8-5.2 ug/L which can be classified as ultrasensitive by standard clinical PSA assay.

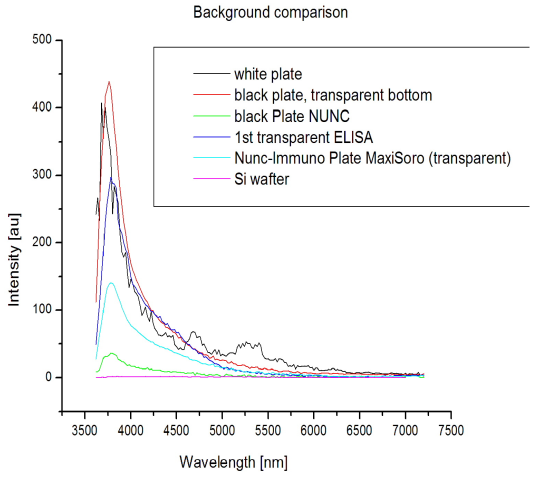

Fig. (5) the comparison between some common plastics used in ELISA plates compared to Si wafer

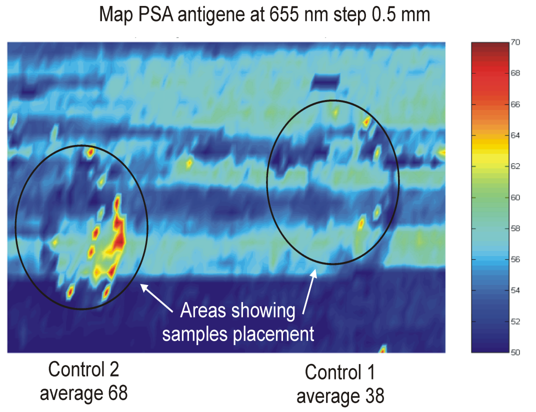

Fig. (6) Mapping of the prepared samples at the 665nm wavelength in the maximum of the QD photoluminescence spectrum

4. Conclusions

QD luminescence biomarkers are detected within the physiological range in plasma. Application of Quantum Dot bioconjugates allowed us to detect antigens below limits of standard tests used in clinics. The use of Silicon as a substrate instead of plastics allowed to further lower the limit of detection of antigen. It also lays the groundwork for a multiplexed biomarker panel by reducing background noise over the entire area of interest to near zero. It was found that the signal from QD's could be enhanced in a controlled manner by using a low power excitation source for some time before the signal is read.

While the results of using Si as a substrate are encouraging there is a need to enhance the method by which biological samples are to be deposited on the Si wafers. Future work will consist of this and the development of cancer biomarker microarrays based on quantum dot bioconjugates.

References

[1] M.A. Hines, P. Guyot-Sionnest, *J. Phys. Chem.* 100, 468 (1996).

[2] M. Bruchez et al., *Science*, 281(5385), 2013, (1998).

[3] E.R. Goldman et al., *Phys. Stat. Sol.* (b) 229 407 (2002)

[4] R.C. Bast Jr. et al., *J. Clin. Invest*,1981. 68(5): p.1331-7

[5] T.J. O'Brien et al., *Amer. J. Obstet. Gynecol.*, 1991. 165(6 Pt 1): p. 1857-64.

[6] T.A. Zhukov, J.L. Kroeger and M.S. Tockman, *Lung cancer biomarker evaluation: Comparison of flow cytometry and laser scanning cytometry in assessment of macrophage migration inhibiroty factor (MIF) expression in lung carcinoma cell lines and sputum specimens.* in *AACR Annual Meeting*. 2004. Orlando, FL

[7] N.E. Korsunska, M. Dybiec, L. Zhukov, S. Ostapenko, T. Zhukov "Reversible and Non-REverible Photo-Enhanced Luminescence in CdSe/ZnS Quantum Dots", *Semicond. Sci. Technol.*, in press

THE IRAQI JOURNAL OF
APPLIED PHYSICS
EDITORIAL BOARD

COPYRIGHT RELEASE
Iraqi Journal of Applied Physics (IJAP)

We, the undersigned, the author/authors of the article titled
…………………………………………………………………………………………………
…………………………………………………………………………………………………
…………………………………………………………………………………………………
…………………………………………………………………………………………………
…………………………………………………………………………………………………
…………………………………………………………………………………………………
that is presented to the Iraqi Journal of Applied Physics (IJAP) for publication, declare that we have neither taken part or full text from any published work by others, nor presented or published it elsewhere in any other journal. We also declare transferring copyrights and conduct of this article to the Iraqi Journal of Applied Physics (IJAP) after accepting it for publication.

The authors will keep the following rights:
1. Possession of the article such as patent rights.
2. Free of charge use of the article or part of it in any future work by the authors such as books and lecture notes without referring to the IJAP.
3. Republishing the article for any personal purposes of the authors after taking journal permission.

To be signed by all authors:

Signature:…………………………………………………..date: ………………………………

Printed name: ………………………………………………………………………………

Signature:…………………………………………………..date: ………………………………

Printed name: ………………………………………………………………………………

Signature:…………………………………………………..date: ………………………………

Printed name: ………………………………………………………………………………

Correspondence address:……………………………………………………………………...
……………………………………………………………………………………………………..
Address:…………………………………………………………………………………………
…………………………………………………………………………………………………
………………………………………………………………………………………………
Telephone:…………………………………..email: …………………………………………..

Note: Please complete and sign this form and mail it to the below address with your manuscript

The Iraqi Journal of Applied Physics
P. O. Box 55259, Baghdad 12001, IRAQ
Website: www.ijap.org
Email: editor@ijap.org
Phone: +964 7901274190

IRAQI JOURNAL OF APPLIED PHYSICS

CONTENTS